Low mass electron pair production at the CERN Proton-Antiproton Collider

Andrea Federspiel

Merano, Italy

A thesis submitted to University of Bern

Laboratory for High Energy Physics

For the degree of Doctor of Philosophy

Dean of the faculty: Prof Dr. E. Schmidt

Supervisor: Prof Dr. J. Schacher

June, 28th 1990

LOW MASS ELECTRON PAIR PRODUCTION AT THE CERN PROTON-ANTIPROTON COLLIDER

Inauguraldissertation
der Philosophisch-naturwissenschaftlichen Fakultät
der Universität Bern
zur Erlangung der Doktorwürde

vorgelegt von

Andrea Federspiel
Meran, Italien

Leiter der Arbeit: Dr. T. Pal und PD Dr. J. Schacher,
Laboratorium für Hochenergie Physik der Universität Bern

Von der Philosophisch-naturwissenschaftlichen Fakultät auf
Antrag des Herrn Prof. Dr. E. Hugentobler angenommen.

Bern, den 28. Juni 1990 Der Dekan:

Prof. Dr. E. Schmidt

Summary

A measurement of the Drell-Yan cross section for the production of electron pairs within the invariant mass interval $10\ GeV/c^2 < M_{ee} < 70\ GeV/c^2$ was performed at the CERN $p\bar{p}$ collider at $\sqrt{s} = 630\ GeV$. The data sample, accumulated by the UA2 detector, corresponds to an integrated luminosity of $7.4\ pb^{-1}$. The cross section obtained is compared with results on muon pair production from the UA1 experiment and with theoretical calculations.

Contents

List of Figures

List of Tables

1 Introduction

The UA2 experiment [1] at the CERN $p\bar{p}$ collider, operating at the centre of mass energy $\sqrt{s} = 630\,GeV$, was upgraded between 1985 and 1987 in order to improve its performance in electron identification and in missing energy measurement. The successful construction and operation of the new Antiproton Accumulator Complex (AAC) enabled the collider to run at peak luminosity of $\approx 3.0{\cdot}10^{30}\ cm^{-2}s^{-1}$.

During the 1988 and 1989 data taking periods, an event sample corresponding to an integrated luminosity of

$\int\mathcal{L}\mathrm{dt} = (7.4\ \pm\ 0.4)\ pb$ [8] was accumulated.

In the following the analysis of the full data sample containing events with two electron candidates is presented.

The thesis is organized in the following way:

In section 2 a brief introduction to the Drell-Yan process is given and in section 3 the UA2 detector with its main characteristics is described. The global track reconstruction and the vertex reconstruction are presented in sections 4 and 5. Section 6 is dedicated to the trigger system, and the following sections include the presentation of the technique used to identify electrons including its efficiencies. Then the description of the Monte Carlo simulations follows.

Finally the last section comprises the goal of this work:

the extraction of the cross section for the Drell-Yan production of electron pairs in the invariant mass interval $10\ GeV/c^2\ <\ M_{ee}\ <\ 70\ GeV/c^2$, for $E_t\ >\ 5.5\ GeV$ and for $E_t\ >\ 6.0\ GeV$, through $p\bar{p}$ collisions at the centre of mass energy $\sqrt{s}\ =\ 630\ GeV$.

2 Drell-Yan process

There are several processes in hadron-hadron collisions in which lepton pairs are produced. Although the individual processes are different in terms of interaction, their resulting invariant mass spectrum shows the same continuum behaviour (exept for the Z^0 production).

The candidate reactions at the parton level are:

1. $q\bar{q} \longrightarrow \gamma^\star \longrightarrow e^+e^-$ (Drell-Yan electron pair production),
2. $q\bar{q} \longrightarrow Z^0 \longrightarrow e^+e^-$ (electron pair production via the decay of the neutral intermediate vector boson).

Also the following reactions produce electron pairs. These reactions are in competition with the Drell-Yan process and are referred to as sources of background:

1. $p\bar{p} \rightarrow B^\pm, B^0, \bar{B}^0 \rightarrow e^+e^- + jet_1, jet_2$ (semileptonic decay of B-mesons),
2. $p\bar{p} \longrightarrow \pi^0, \eta \longrightarrow \gamma e^+e^-$ (Dalitz decay background).

The direct production of lepton pairs with large invariant masses via the quark-antiquark annihilation was studied originally by Drell and Yan in the year 1970 [11].

The first observation of massive lepton pairs produced in hadron collisions was reported by Christenson et al. [3], and Drell and Yan were then able to interprete the falling invariant mass spectrum of the lepton pairs.

With the evolution of the "naive" [1] parton model in a description including QCD[2] effects, the Drell-Yan process continued to play an important role in hadron physics. A typical example is the production of the intermediate vector bosons Z^0 and $W^\pm$.

In the original Drell-Yan mechanism a quark and an antiquark annihilate to yielding a virtual photon $\gamma^\star$. For invariant masses $M_{ee} < M_Z$ the annihilation process is mainly of electromagnetic nature and therefore the corresponding cross section is provided by QED together with corrections from QCD.

[1] For a more detailed description of the "naive" parton modell, see C. Grosso-Pilcher et al., Ann.Rev. Nucl.Part.Sci. 1986, 36. 1-28 .

[2] Quantum Chromo Dynamics.

2.1 Kinematics of the process

Drell and Yan [12] proposed a simple electromagnetic process to account for the production of the continuum of dilepton pairs from hadron-hadron collisions:

$$H_1 + H_2 \quad \longrightarrow \quad (q\bar{q} \quad \longrightarrow \quad \gamma^\star) \quad \longrightarrow \quad l^+ l^- + X. \tag{1}$$

H_1 and H_2 are the interacting hadrons.

The essential steps are the annihilation of a quark from one hadron and an antiquark from the other hadron yielding a virtual photon and the decay of the virtual photon into a pair of leptons.

The other components of the hadrons can be treated as spectators, where they rearrange themselves by fragmentation into outgoing hadrons.

The 4-vector for the colliding hadrons are:

$$\begin{aligned} p_1 &= \frac{\sqrt{s}}{2}(1,0,0,1), \\ p_2 &= \frac{\sqrt{s}}{2}(1,0,0,-1), \end{aligned} \tag{2}$$

where $\sqrt{s}$ is the centre of mass energy.

p_1 and p_2 represent the proton and antiproton momenta along the z-coordinate.

The energy-momentum conservation yields for the four-momentum of the $\gamma^\star/Z^0$:

$$p^{\gamma^\star/Z^0} \;=\; \hat{p_1} \;+\; \hat{p_2}, \tag{3}$$

where $\hat{p_i} \;=\; x_i p_i \quad (i = 1, 2)$,

and correspond to the parton four-momenta.
The parton i carries the fraction x_i of the proton/antiproton four-momentum.

According to equation (2) the following relations for the energy and momentum of $\gamma^\star$ emerge:

$$\begin{aligned} E^{\gamma^\star} &= \frac{\sqrt{s}}{2}(x_1 + x_2), \\ p_L^{\gamma^\star} &= \frac{\sqrt{s}}{2}(x_1 - x_2). \end{aligned} \tag{4}$$

Here $p_T^{\gamma^*} = 0$ is assumed, *i.e.* the partons have a negligible amount of transverse momentum inside the proton/antiproton.
The invariant mass of an electron pair is given by:

$$M_{ee}^2 = \left(E^{\gamma^*}\right)^2 - \left(p_L^{\gamma^*}\right)^2, \\ = s x_1 x_2. \tag{5}$$

There exists two basic relations between the quark variables and the observables:

$$\tau = \frac{M_{ee}^2}{s}, \\ = x_1 x_2. \tag{6}$$

$$x_f = \frac{2p_L^{\gamma^*}}{\sqrt{s}}, \\ = x_1 - x_2. \tag{7}$$

x_f is the Feynman variable also called scaling variable.

The process (1) can be represented by the following diagram:

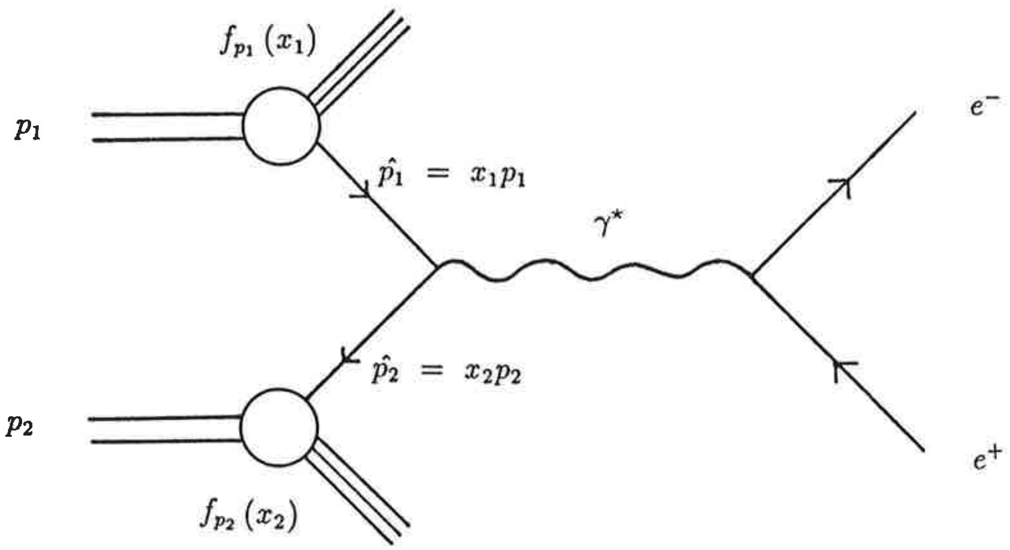

Figure 1: Feynman diagram for the Drell-Yan process.

2.2 Lowest order cross section

The cross section of the Drell-Yan process in lowest order, i.e. "Born approximation", can be written in the following form:

$$\sigma\left(q_k\bar{q}_k \rightarrow e^+e^-\right) = \frac{1}{N_c}\frac{4\pi\alpha^2}{3\hat{s}}e_k^2, \tag{8}$$

where α is the fine structure constant, e_k is the electric charge of the quark and $\hat{s} = sx_1x_2$ is the invariant mass squared of the subsystem. N_c is the number of colours.

The equation of the differential cross section is

$$\frac{d\sigma}{dM^2}\left(p\bar{p} \rightarrow eeX\right) = \frac{4\pi\alpha^2}{N_c 3M^2 s}\int\frac{dx_1}{x_1}\frac{dx_2}{x_2} \cdot\left(\sum_k e_k^2\left[q_k\left(x_1\right)\bar{q}_k\left(x_2\right)+\left(1\leftrightarrow 2\right)\right]\right)\delta\left(1-z\right), \tag{9}$$

where

$$z = \frac{M^2}{x_1x_2s}. \tag{10}$$

$q_k\left(x_1\right)$ is called the scaling density and represents the probability of finding a quark in hadron 1 in the fractional momentum interval $x_1 \cdots x_1 + dx_1$. The sum is taken over all possible quark flavours. The δ function provides the selection of the adequate values for the kinematical variables x_1 and x_2.

Hidden in the differential cross section is a factor M^{-4} responsable for the rapid fall of the differential cross section with increasing dilepton mass.

The cross section is divergent for $M \rightarrow 0$.

2.3 Higher order QCD calculations and the K-factor

In the QCD improved parton model, the differential cross section (9) is modified by strong interaction effect, *i.e.* gluon radiation has to be considered.

The differential cross section has then the form [12]:

$$\begin{aligned}\frac{d\sigma}{dM^2}(p\bar{p} \rightarrow eeX) &= \frac{4\pi\alpha^2}{N_c 3M^2 s}\int\frac{dx_1}{x_1}\frac{dx_2}{x_2} \\ &\{\sum_k\left[\left[e_k^2\left(q_k\left(x_1\right)\bar{q}_k\left(x_2\right)\right)\right]+[1\leftrightarrow 2]\right]\left[\delta\left(1-z\right)+\frac{\alpha_s}{2\pi}f_q\left(z\right)\right]+ \\ &\sum_k\left[\left[e_k^2\left(g\left(x_1\right)\left(q_k\left(x_2\right)+\bar{q}_k\left(x_2\right)\right)\right)\right]+[1\leftrightarrow 2]\right]\left[\frac{\alpha_s}{2\pi}f_g\left(z\right)\right]\}. \quad (11)\end{aligned}$$

The non-leading correction terms are included in the functions $f_q(z)$ and $f_g(z)$.

The $\mathcal{O}(\alpha_s)$ corrections to the cross section have been computed long ago [13] and found to be large.
These corrections are subdivided into *"virtual corrections"* and *"real corrections"* .

The Feynman diagrams corresponding to the *"virtual corrections"* are given below:

$q\bar{q} \longrightarrow \gamma^*$:

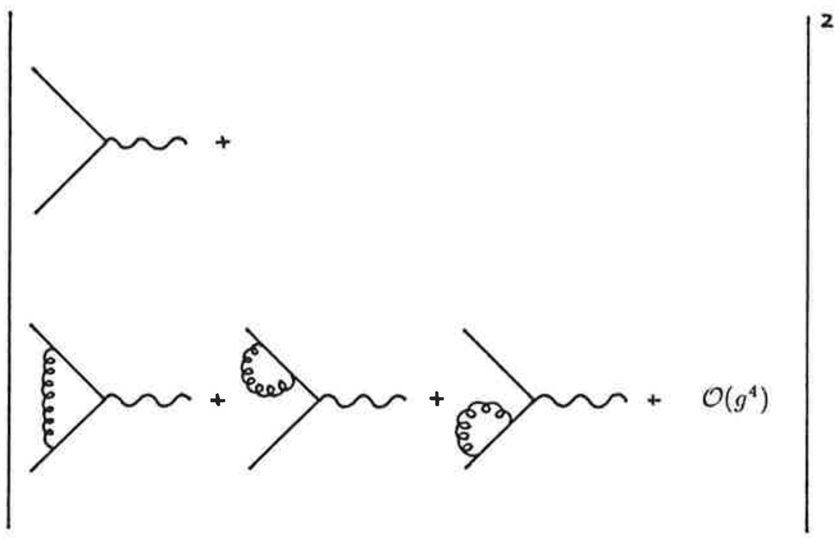

Figure 2: Feynman diagrams corresponding to the *"virtual corrections"* in $\mathcal{O}(\alpha_s)$.

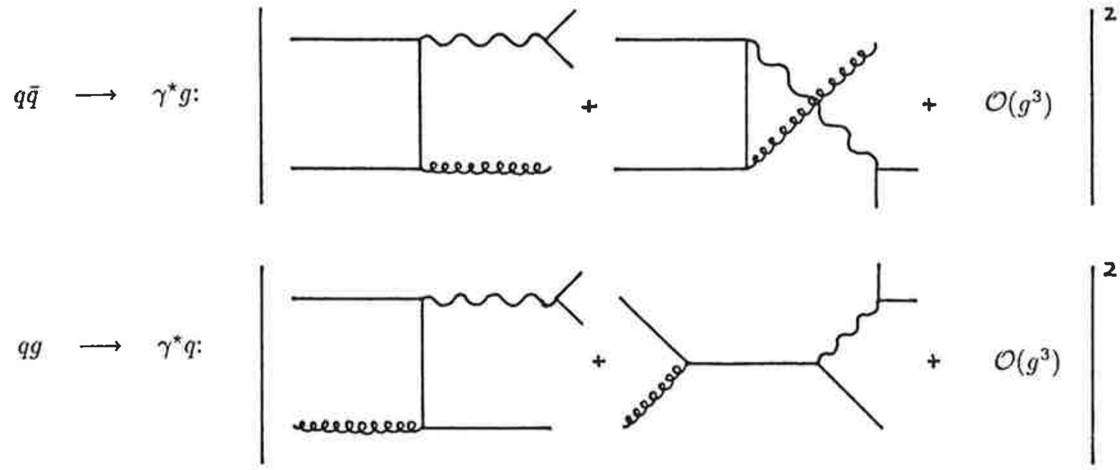

Figure 3: Feynman diagrams corresponding to the *"real corrections"* in $\mathcal{O}\ (\alpha_s)$.

The ratio of the corrected to the lowest order cross section

$$K = \frac{\sigma_{corrected}}{\sigma_{lowest\ order}} \tag{12}$$

is called the K-factor [23] for the Drell-Yan process.

It includes the non-leading corrections and in particular these which cannot be precisely expressed by analytical formula.

Recently the calculation of an important part of the two loop K-factor has been completed [22].

For the $\mathcal{O}\ (\alpha_s^2)$ the K-factor depend on the variable τ and its value is $K \approx 1.65$ for $\sqrt{s} = 630\ GeV$ at $M_{ee} = 10\ GeV/c^2$.

The factor is also slowly varying with M^2.

3 UA2 detector

A perspective view of the UA2 detector at the CERN $p\bar{p}$ collider is given in figure 4. Figure 5 shows a cross section of the UA2 calorimeter.

The detector is subdivided into two main regions: The central calorimeter covering the pseudorapidity (η) region $|\eta| \leq 1$ includes electromagnetic and hadronic compartments. The region of $1 < |\eta| < 3$ is covered by the end-cap calorimeters, which are also subdivided into electromagnetic and hadronic compartments.

Each calorimeter region is preceeded by a preshower detector providing stereo tracking: the scintillating fibre detector (SFD) in the central part, and the end-cap proportional tubes detector (ECPT) in the forward region.

As shown in figure 6, the SFD detector is the outer-most part of the cylindrical central detector which fits into the central calorimeter. In addition the following devices are also in the central detector:[3]

1. the "inner" silicon hodoscope (ISI),
2. the jet vertex detector (JVD),
3. the "outer" silicon detector (OSI),
4. the transition radiation detector (TRD).

In the forward region there are two time-of-flight hodoscopes (TOF) close to the Beryllium beam pipe.

Beryllium, as beam pipe material, is chosen instead of corrugated stainless steel because of the following reasons:

- The diameter of the beam pipe can be reduced to 60 mm with a thickness of 0.9 mm.
- The number of radiation length for traversing particles can be reduced by a factor 5. This reduces the rate of photon conversion and delta-ray production.

In the following sections each part of the detector is described, starting from the centre of the UA2 apparatus.

[3] The sequence of the detectors cited describes the position, starting from the centre of the apparatus.

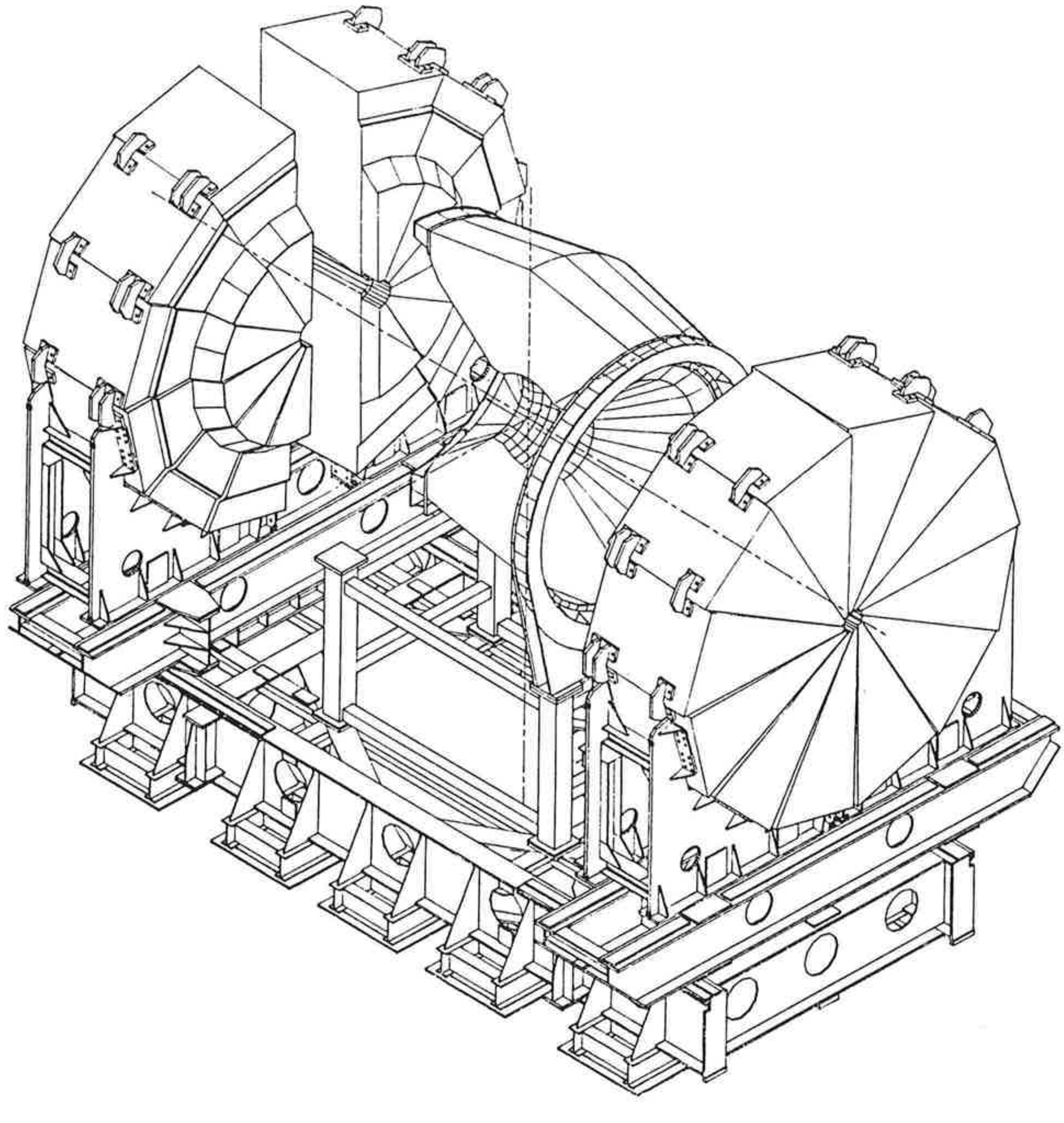

Figure 4: A perspective view of the UA2 detector.

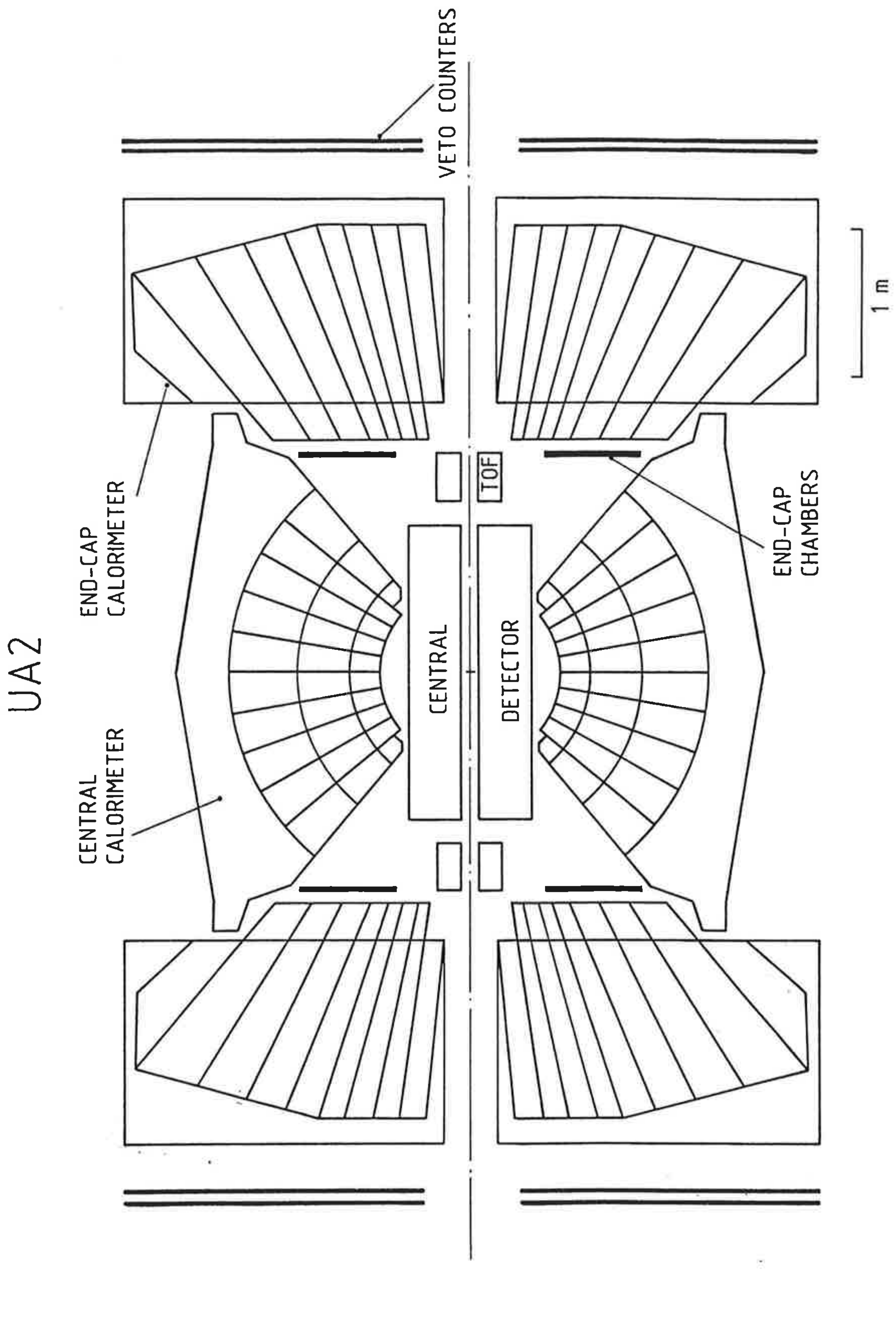

Figure 5: Cross section of the UA2 detector.

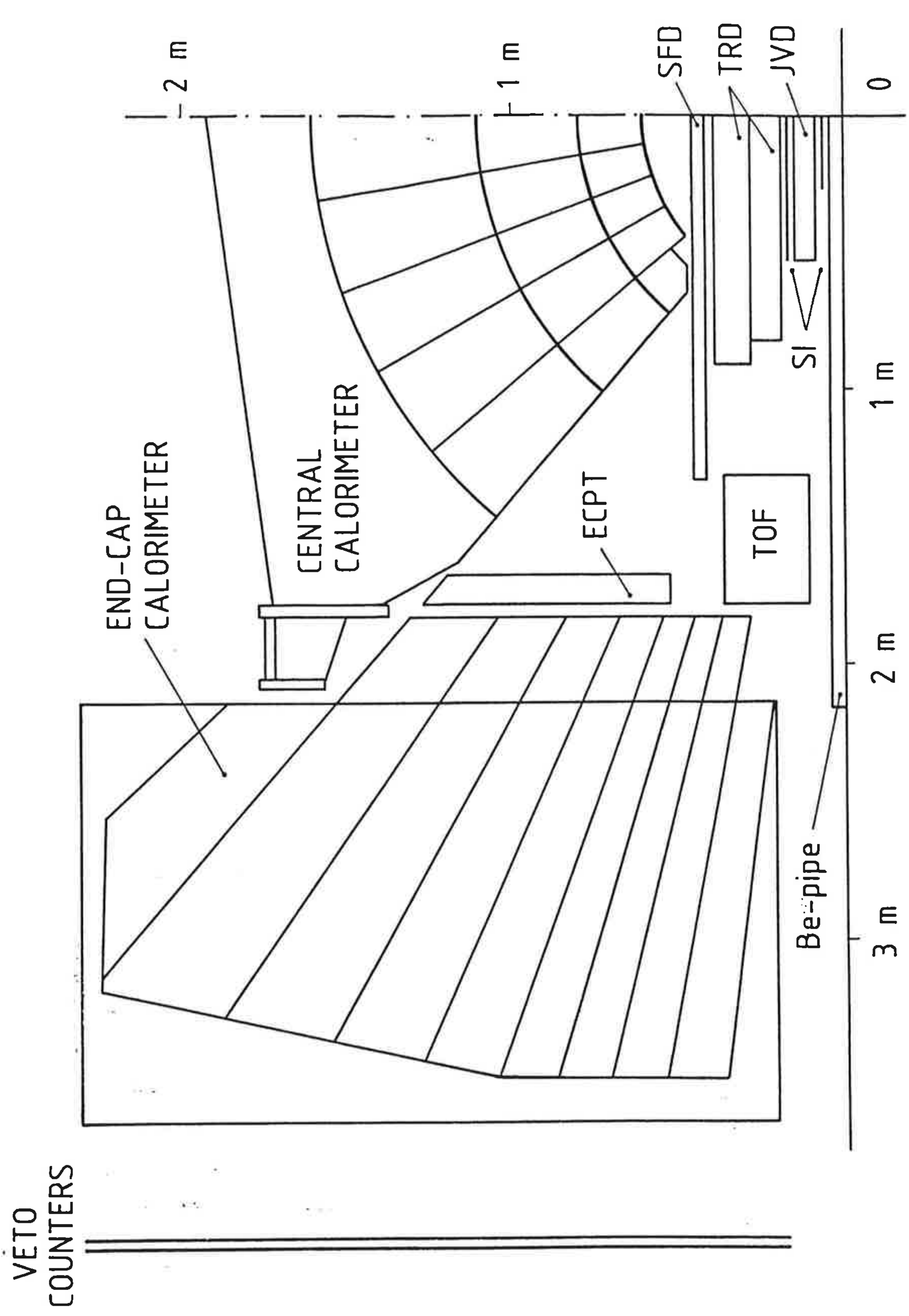

Figure 6: A detailed view of the UA2 detector with the calorimeters and the central tracking detectors.

3.1 Inner Silicon Hodoscope (ISI)

The inner silicon hodoscope (ISI) [4] is the most inner placed detector in the UA2 apparatus and fits into a space between two cylinders with diameters of 56 mm and 67 mm. Since points along a track are measured by the Jet Vertex Detector (JVD)[4] and by the Scintillating Fibre Detector (SFD)[5] with accuracy, the detailed and complex evaluation of the data from these detectors is a time consuming process, in particular in the case of multivertex events.

In contrast, the information of the ISI, together with that of the OSI detector, allows for fast track finding algorithms.

The ISI consists of 192 silicon counters arranged in 12 rows of 16 crystals each. The dimensions of the crystals are $17.3 \times 33.5\ mm^2$, with 16 pads of 2 mm pitch separated by 200 μm oxide. The thickness of the crystal is $\sim 300\ \mu$m. The counters of one row overlap with those of the next row to achieve full coverage. All rows are fixed to a Carbon fibre support cylinder around the beam pipe. The counters are mounted on a multilayer printed circuit board made of fibreglass and Capton layers. This board also supports an Application Specific Integrated Circuits (ASIC), a chip containing the electronics for 16 channels.

The complete electronics chain consists of a charge-sensitive preamplifier, shaping amplifier, track-and-hold and analog multiplexing circuit. The 16 channel ASIC chip (called Amplex) has been developed at CERN in collaboration with industry. The performance and characteristics of the Amplex chip were measured at CERN and Bern. The program included the measurement of the gain, gain uniformity, noise, linearity, power consumption and peaking time of the shaper.

The characteristics of the crystals were studied at CERN, Cambridge and Perugia. The aims were the determination of the crystal leakage current which is on average 5 nA/pad, and the evaluation of the depletion voltage for each pad (which ranges generally from 30 to 40 V). Figure 7 shows a photograph of the ISI detector, with one individual board at the side. The details of the board and mounting scheme are shown in the upper picture.

---

[4]See next section.

[5]See section 3.4 for a precise description.

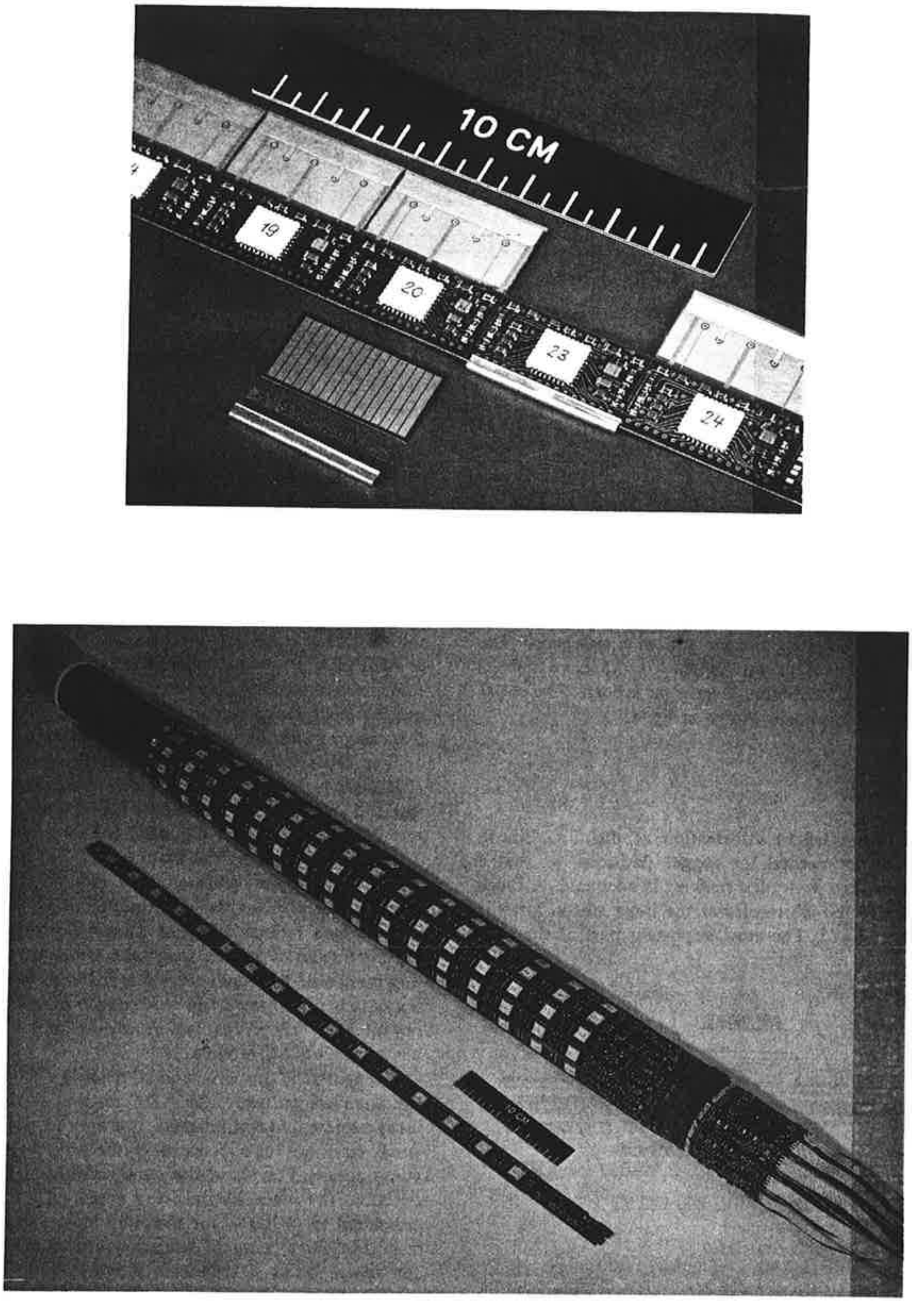

Figure 7: Photograph of the ISI detector, with one individual board at the side. The details of the board and mounting scheme are shown in the upper picture.

3.2 Jet Vertex Detector (JVD)

The jet vertex detector (JVD) [5], is a cylindrical drift chamber around the beam pipe with a total of 1.5% of a radiation length. The purpose of the JVD is to determine the direction of all charged particles with high resolution and efficiency. The sensitive volume is 1 m long and spans from 40 to 124 mm in radius. The chamber consists of 16 sectors with 13 sensitive layers each. The sense wires are interleaved with guard wires, whilst two planes of cathode wires provide the electric isolation from nearby sectors. All guard wires are held at the same potential of ~ -1400 V. The sense wires are grounded. Signals are first preamplified and further amplified by circuits which also provide pulse shaping. A FASTBUS 100 MHz six-bit FADC system provides the digitization.

The space coordinates of the charged particle tracks are determined offline by combining the drift-time and the signal charges at both ends of the sense wires.

3.3 Outer Silicon Detector (OSI)

The main purpose of the outer silicon detector (OSI) [6] is to provide additional rejection against π^0 Dalitz decays and photon conversion (an important source of background).

The second major aim of the detector is to provide an online capability of space point information as discussed already in the previous section 3.1 .

The array consists of 432 silicon counters which are arranged in groups of 9 on 48 modules [6] covering the polar angle range $25^0 < \theta < 155^0$ over the full azimuth. Each counter is subdivided into 7 pads of 8.7 × 40 mm^2 separated by 100 μm oxide strips. The thickness of the counters are ~ 300 μm. The modules are supported by a carbon fibre cylinder mounted around the JVD detector.

The signal from each pad is transfered to a low-noise preamplifier on the motherboard then to the shaper, track-and-hold circuit and multiplexer. The complete electronics part is cooled in order to avoid overheating of the detector. The crystals operate in a nitrogen atmosphere.

The characteristics of the electronics chain were measured at Bern and the crystals at CERN; in particular the leakage current of the crystals were found to be in avarage ~ 50 nA/pad .The depletion voltage was typicaly ~ -20 V for high resistivity crystals and ~ -80 V for low resistivity crystals.

A schematic view of the OSI detector is shown in figure 8.

[6]The modules are called motherboards.

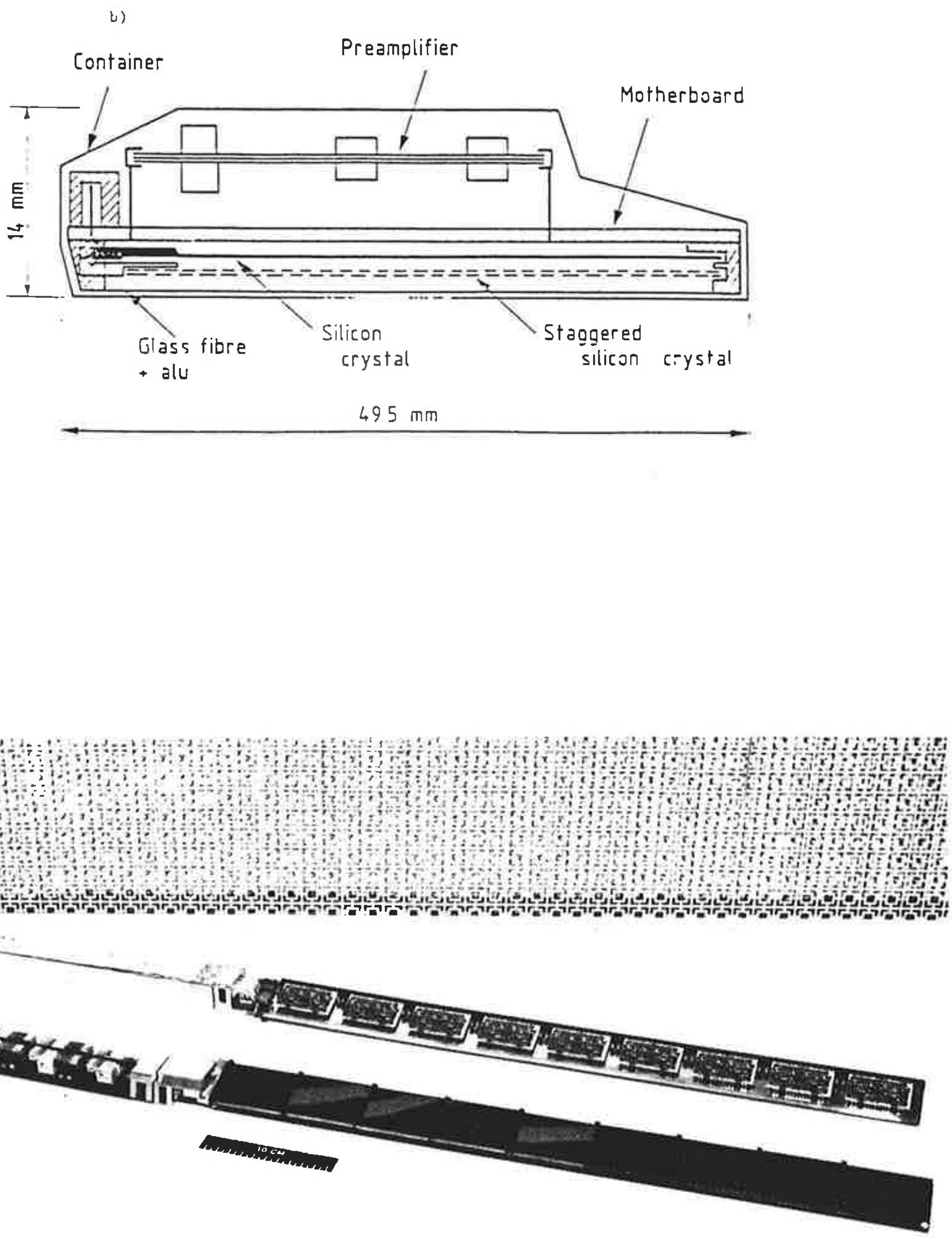

Figure 8: Photograph of the fully assembled motherboard with the associated electronics box. The layout of the OSI is shown above.

3.4 Transition Radiation Detector (TRD)

The aim of the transition radiation detector (TRD) is the efficient detection of high energy electrons. The detector is formed of concentric cylinders each consisting of a stack of radiators followed by a xenon filled chamber. When an electron passes through the stack, X-rays are produced by transition radiation [2].

The chambers are built asymmetric. Between the window (-1000 V) and the grid (at ground) there is a long drift space followed by the amplification space with a high field gradient between the grid and the signal wires (at + 1500 V). The signal wires are separated by field wires (at +50 V).

Electrons produced by the X-rays in the chamber drift towards the sense wires and the arrival time is a measure for the production position. Charged pions produce ionisation in the chamber. Electrons also produce ionisation but in addition X-rays photons which are absorbed by the Xenon in the early part of the chamber. These cause large signals at late times.

3.5 Scintillating Fibre Detector (SFD)

The purpose of the scintillating fibre detector (SFD) [9] is summarized as follows:

- track information near the central calorimeter obtained from the stereo projections,
- the localization of the beginning of the electromagnetic shower, generated in the radiator by electrons or photons.

This detector provides extra rejection against the background coming from the overlap of charged pions with photons which could fake an electron in the calorimeter.

For a more detailed description of the SFD detector see the reference cited above.

3.6 Central Calorimeter

The UA2 detector is instrumented to identify electrons with good energy resolution in the electromagnetic calorimeter and hadronic jets by the hadronic calorimeter. Both parts have the same cell structure and allow to detect electrons and jets in the same apparatus.

The calorimeter, which covers the region in polar angle of $40^0 \leq \theta \leq 140^0$ over the full azimuth, is segmented into 240 cells, each cell covering 10^0 in polar angle and 15^0 in azimuth. The distance of each cell from the centre of the $p\bar{p}$ interaction region to the front face of the cell is constant, and is 600 mm. In order to achieve good energy resolution for both electrons and hadron jets (and discrimination between electrons and hadrons), the electromagnetic part of the calorimeter is made of a lead-scintillator sandwich and the hadronic one is made of a iron-scintillator sandwich. The light is collected by wave length shifters and light guides arranged between the cells. The phototubes are mounted at the back of the module in light-tight mountings. Figure 9 shows schematically the construction of one calorimeter cell.

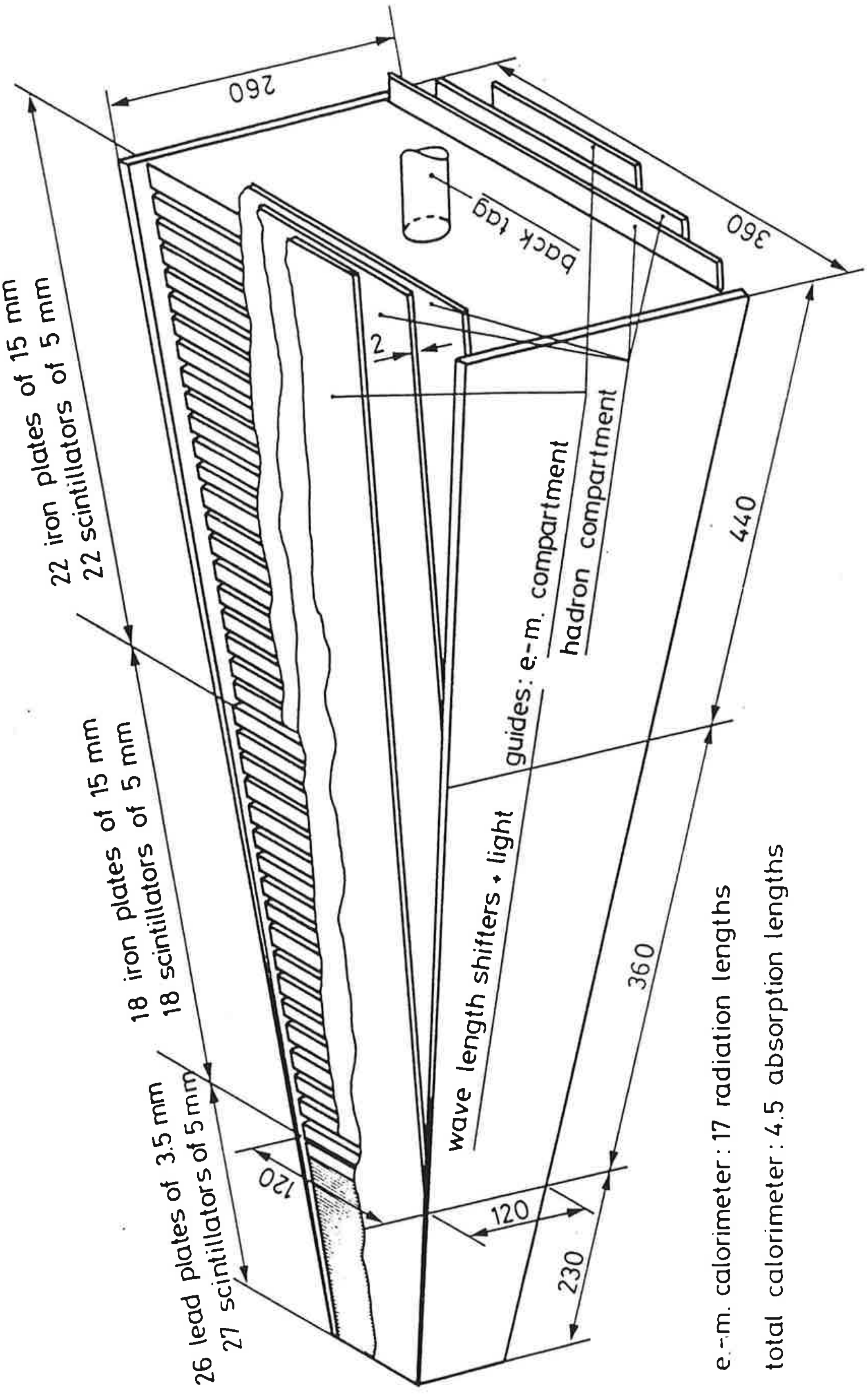

Figure 9: The calorimeter cell with the electromagnetic and hadronic compartments.

The energy calibration and the stability of the calorimeter is checked by:

1. test beam measurements:

   each of the 24 modules was calibrated before installation in the UA2 apparatus using a 10 GeV beam of e^- and using 10 GeV μ^- for the hadronic compartments.

2. ^{60}Co source measurement:

   the measurement of the direct current induced by a ^{60}Co source is an independent way to monitor the calibration of the electromagnetic calorimeter cells. This measurement is done periodically.

3. "Energy flow" measurement using minimum bias events from $p\bar{p}$ collisions:

   this measurement is a further check of the calibration of each cell of the electromagnetic calorimeter. It uses the average "energy flow" into each cell.

The information on the stability of the calorimeter is obtained by recalibrating a part of the calorimeter which, for this purpose, had to be dismounted. The recalibration shows an overall decrease of the response to particles of a given energy. For each module the average drift in the electromagnetic calorimeter for 10 GeV e^- is of the order of ~ 7 % per year. In order to determine the energy scale, the modules in the test beam setup were exposed to e^- beams of different incident energy. Furthermore, scans over the surface of each cell were made in order to check the uniformity. The test beam energies available were 20, 40 and 80 GeV.

All cells in the polar angle range $40^0 \leq \theta < 50^0$ and $130^0 < \theta \leq 140^0$ were modified during the UA2 upgrade. These cells will be referred to as *edge cells (EC)* (cells 1 and 10) hereafter.
The cells in the polar angle range $50^0 \leq \theta \leq 130^0$ are called *central cells (CC)* (cells 2 to 9) hereafter.

3.7 End Cap Proportional Tubes (ECPT)

In order to provide tracking in the forward regions, and to observe the initiation of electromagnetic showers produced by electrons and photons, a set of proportional tubes are installed in front of the end cap calorimeters [7]. Each ECPT detector is divided into eight 45^0 azimuthal sectors. The chambers cover the polar angle range $22.5^0 < \theta < 37.5^0$. Each module consists of 6 planes of tubes for particles tracking, iron-lead converter and 3 planes of tubes for detecting preshowers produced in the converter. The 613 tubes of each sector operate in proportional mode and are read out through a track-and-hold and multiplexing scheme similar to the one used for the silicon hodoscopes. The complete electronics parts were built and tested at Bern. The Bern and Pavia groups are responsable for the ECPT detector.

3.8 End Cap Calorimeters

The angular coverage of the end cap calorimeters is $1 < |\eta| < 3$. The end cap calorimeters employ the same technique as the central calorimeter (Pb and Fe absorber plates with scintillator and wave length shifter read-out) with similar cell granularity and sampling fractions. The two cells closest to the beam axis cover 30^0 in azimuth. The other end cap cells have a constant segmentation of $\Delta\phi = 15^0$ and $\Delta\eta = 0.2$. All cells in $1.0 < |\eta| < 2.5$ have one electromagnetic and one hadronic compartment and the cell closest to the beam has only one hadronic compartment. In order to ascertain a good (E_t) measurement, additional hadronic calorimeter cells have been installed in the pseudorapidity interval $0.9 < |\eta| < 1.0$, overlapping with the edge cells of the central calorimeter , to measure particles escaping from the interface between the end caps and the central calorimeter. Furthermore each end cap module ($\Delta\phi = 30^0$) is tilted by an angle of 15 $mrad$ with respect to the plane perpendicular to the beam axis, in order to avoid an alignment of the dead space occupied by the wave length shifter read out plates with the event vertex.

The energy resolution σ_E for electromagnetic showers is typically
$17\ \% \cdot \sqrt{E}$ with E in GeV.

For a more detailed description of the end cap calorimeters see reference [1].

4 Global track reconstruction

The UA2 detector has no magnetic field. Each particle, produced in the $p\bar{p}$ collision at one "a priori" unknown vertex point, moves from the vertex outwards. A set of tracks are reconstructed from the information of the different detectors together with the information of the calorimeters. An algorithm then defines a "global track" referring to only one track with the highest probability of being the track corresponding to an electron candidate.

The tracking efficiency for isolated tracks was measured to be

$$\varepsilon_{tracking} = (90.6 \pm 0.8 \pm 0.8)\ \%, \qquad (13)$$

using a sample of electrons produced in the decay of $W^{\pm}$ bosons [8]. The error quoted first is the statistical error and the error quoted second is the systematic error.

5 Vertex reconstruction

The position of the event vertices along the beam axis were reconstructed using the information of the SFD detector in conjunction with the information of the silicon hodoscopes and the JVD. A vertex finding program searched for up to three vertices per event. The inefficency for finding the highest multiplicity vertex, once an electron track was found, is found to be negligible for vertices within 250 mm of the detector centre. Vertices beyond 250 mm were rejected. The fraction of vertices inside this cut is [8]

$$\varepsilon_{vertex} = (94.3 \pm 0.5)\ \%. \qquad (14)$$

6 Data acquisition system (DAQ)

Due to the high luminosity of the collider the design of a sophisticated trigger system to master the high event rate was one of the most challenging tasks.

The decision whether to accept or reject an event must occure within 3.8 μs, *i.e.* the beam structure of the $p\bar{p}$ collider.

In the case of the UA2 detector, the trigger system consists of one hardware and two software triggers, called level_1 level_2 and level_3. Only a fraction of all events produced in the $p\bar{p}$ collision are events with two electron candidates. The relevant trigger to select these events is called the *"Z - trigger"* and has the following characteristics:

- The level_1 trigger uses the analog information of the calorimeter. Decisions are made in less than 1.5 μs between the bunch crossing. Therefore no deadtime is introduced. At this stage a fast digitization of the calorimeter information is started. For the *"Z-trigger"* all possible combinations of electromagnetic $2 * 2$ cell clusters are investigated. Two clusters must exceed 5 GeV in transverse energy (E_t) and must be separated in azimuth by $\Delta\phi \geq 60^0$. This trigger must also be in coincidence with a minimum bias trigger which is based on a relative arrival time of the particles from the $p\bar{p}$ collision. This time is measured by the time-of-flight hodoscopes (TOF), which are situated on each side of the collision point.
- The level_2 trigger consists of a special trigger processor known as XOP (eXtended Online Processor) which provides a decision, including the digitization of the fast input stream, in less than 1 ms. The software implemented in the XOP contains the following cuts:
  1. The cluster radius in cell units must be $R_{cluster} \leq 0.6$,
  2. The hadronic leakage must be[7]

$$\frac{E_H}{E_{tot}} \leq 1.5\ [0.023\ +\ 0.034\ ln\ (E_{tot})]\,. \tag{15}$$

- The level_3 is implemented in a pool of general purpose FASTBUS processors. At this stage the information of the calibration constants are also available and together with the pedestals the decision can be made more precisely.

It should also be mentioned that the DAQ system described above plays an important role in the error reporting, run control and performance monitoring.

Once an event passed all the different trigger levels it is recorded on a IBM 3480 cartridge via a VAX 780.

In the offline analysis the "CALELE" requirement is the combination of the level_1 and level_2 conditions.

[7] 1.5 is the proportionality factor for leakage for central calorimeter cells 2 - 9, whereas for cells 1 and 10 the factor is 3.0.

6.1 Trigger efficiencies

For the case of electron pairs with low E_t, the investigation of the trigger efficiencies is important because of threshold effects.

6.1.1 Level_1 efficiency

For the calculation of the level_1 trigger efficiency one can profit from the fact, that the data acquisition system provides a *"Z-trigger"* bit for all events with two electromagnetic clusters (EM) separated in azimuth by $\Delta\phi \geq 60^0$. These events are called "Z-events". If both clusters pass the E_t cut, this bit remains activated, otherwise it is reset. The efficieny for the level_1 trigger is defined as

$$\varepsilon_{level\_1}(E_t) = \frac{A}{A+B} \tag{16}$$

with

A = number of "Z-events" with two EM clusters satisfying the E_t cut,

B = number of "Z-events" without two EM clusters satisfying the E_t cut,

A+B = total number of events.

The error calculation gives

$$\Delta\varepsilon_{level\_1}(E_t) = \sqrt{\frac{\varepsilon(1-\varepsilon)}{A+B}} \tag{17}$$

where $\varepsilon = \varepsilon_{level\_1}(E_t)$ as calculated in equation (16).

For the evaluation of the level_1 efficiency ≈1500 events were analyzed. The dependence of the trigger efficiency on E_t is shown in figure 10.

Note that, because of aging effects of the calorimeter, there is a smearing of E_t at level_1.

6.1.2 Level_2 and level_3 efficiencies

For the study of the level_2 and level_3 efficiencies "special" runs were recorded at the end of the 1989 running period at low luminosity and correspond to a total data sample of ≈3000 events. The running conditions were set in such a way that the rejection at level_2,3 was inhibited. Similarly to the previous determination of the efficiency, the available bits were used for the calculation of the level_2,3 efficiencies. The following relation is used:

$$\varepsilon_{level\_2,3}\left(E_t\right) = \frac{A}{A+B} \tag{18}$$

with

A = number of events with 2 electromagnetic clusters separated by an azimuthal angle $\geq 60^0$ and with the level_1, level_2 and level_3 bits set,

B = number of events with 2 electromagnetic clusters separated by an azimuthal angle $\geq 60^0$. The level_1 or level_2 or level_3 bits are not set,

A+B = number of events with 2 electromagnetic clusters separated by an azimuthal angle $\geq 60^0$.

The error is given by

$$\Delta\varepsilon_{level\_2,3}\left(E_t\right) = \sqrt{\frac{\varepsilon\left(1-\varepsilon\right)}{A+B}}, \tag{19}$$

where

$\varepsilon = \varepsilon_{level\_2,3}\left(E_t\right)$ as calculated in equation (18).

Figure 11 shows the dependance of the level_2,3 efficiencies on E_t.

6.1.3 Parametrization of the level_1,2,3 trigger efficiency

A parametrization of the overall trigger efficiency is desirable in order to reduce statistical errors instead of removing all events below some threshold in E_t. For this purpose the shape of the efficiency is fitted to a quadratic polynomial which is thought to be a sufficient approximation for a fit to the data.

$$\varepsilon_{level\_1,2,3}^{fitted} = a + b \cdot E_t + c \cdot (E_t)^2 \qquad (E_t \; in \; GeV)\,. \tag{20}$$

The fit is not done over the full E_t range of the spectrum but only in the restricted E_t-region between 4.8 GeV and 6.3 GeV. From 6.3 GeV to 8.0 Gev in E_t the fit function is set artificially to 1.0. In figure 12 the fit function is superimposed onto the data.

The fit-procedure yields for the coefficients the following values:

Table 1: The coefficients for the fit to the overall trigger efficiency.

a	=	-9.784
b	=	3.108
c	=	-0.222

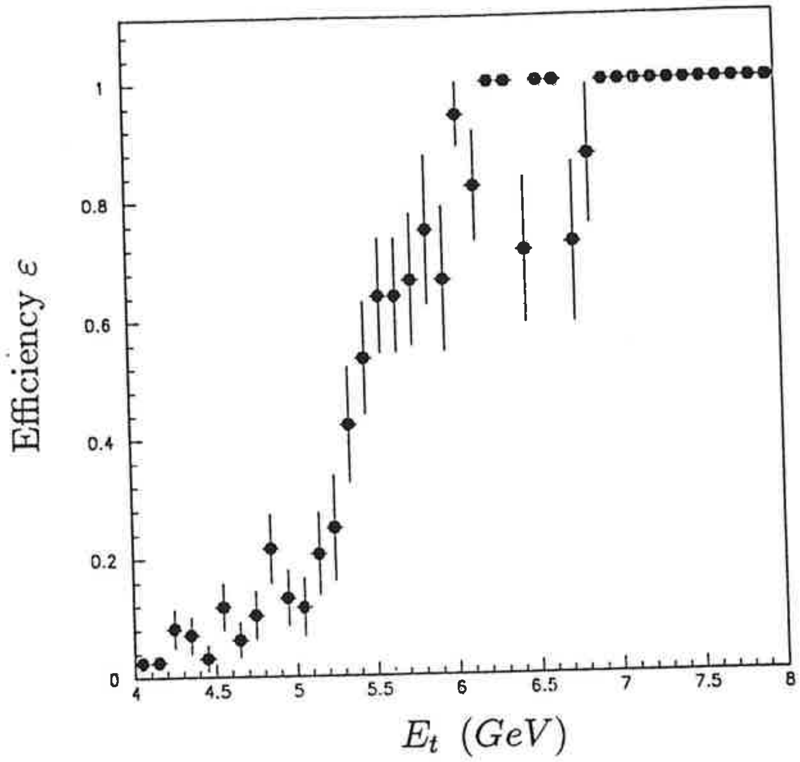

Figure 10: The level_1 trigger efficiency.

Figure 11: The level_2,3 trigger efficiencies.

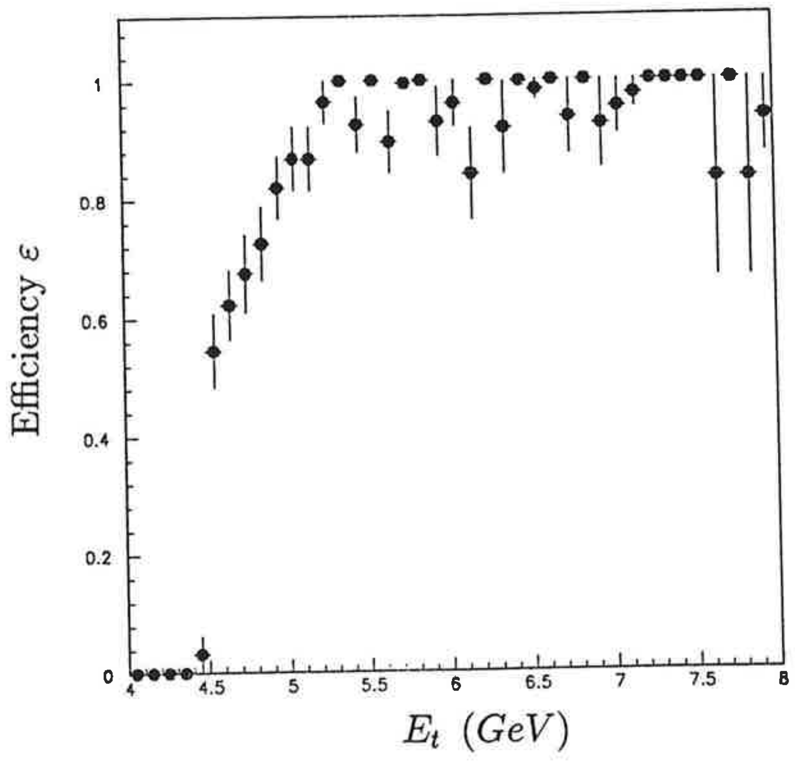

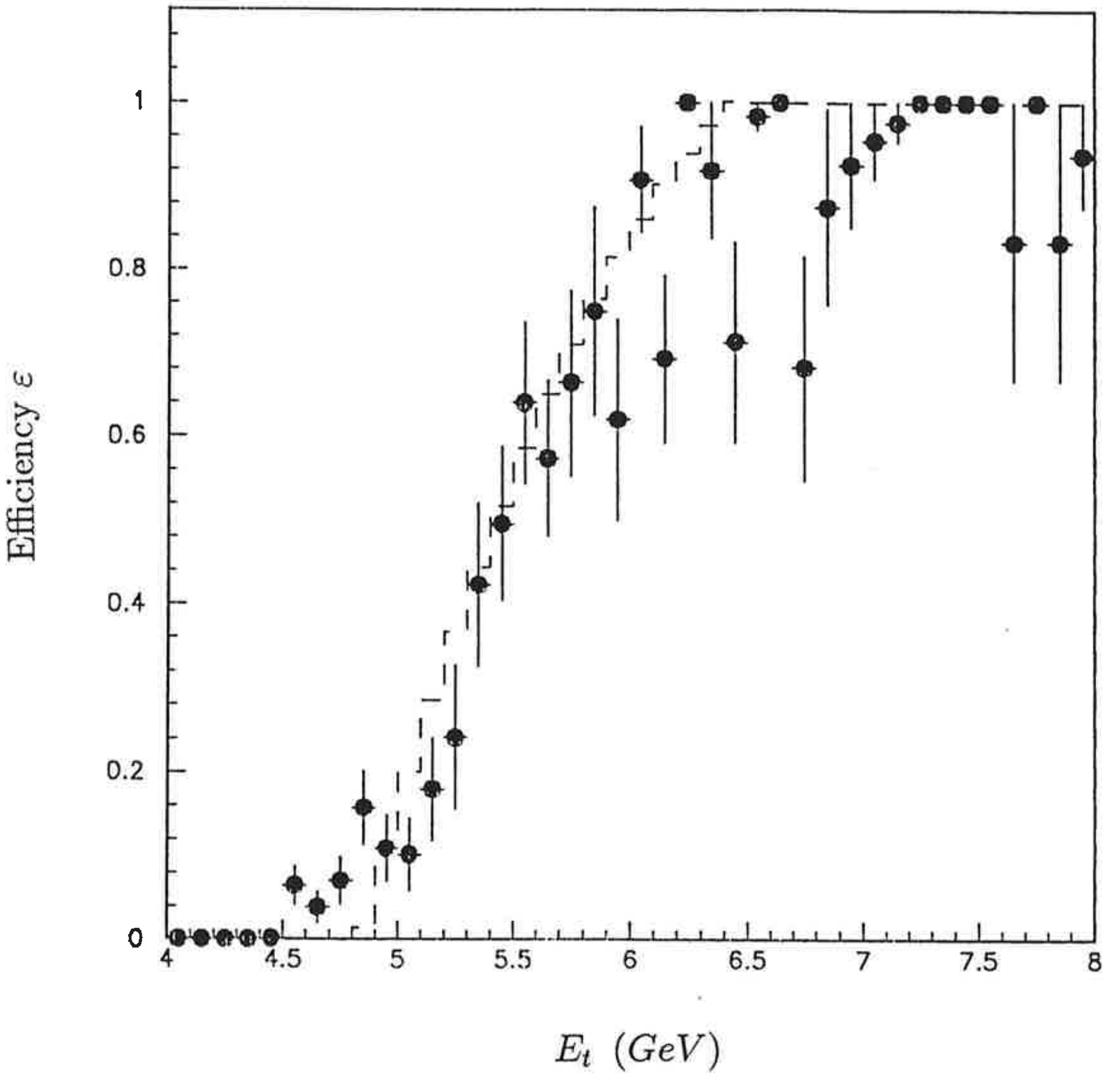

Figure 12: The level_1,2,3 trigger efficiencies (points) with the fitted function (dashed line) superimposed.

7 Energy reconstruction and energy scale

Each cell of the central calorimeter is divided into one electromagnetic and two hadronic compartments as pointed out in section 3.6. In the case of two-electron events the trigger system requires the presence of two electromagnetic cell clusters satisfying the CALELE conditions.

The UA2 software incorporates a set of routines dedicated to the reconstruction of the energy measured by the calorimeter cells. These routine are called ERIC from here onwards. The algorithm used in ERIC takes into account:

1. the impact point of the particle at the cell surface,
2. the energy spread into 8 cells surrounding the hit cell,
3. The leakage of energy into the hadronic compartments of the cells by evaluating the ratio E_{H1}/E_{total},
4. the energy loss of the electron candidate in the $SFD_{preshower}$ detector,
5. the attenuation length of the BBQ's.

An electromagnetic shower produced in the converter of the $SFD_{preshower}$ detector by an electron candidate has, at the surface of a calorimeter cell, a specific lateral shower distribution. Therefore the electron candidate energy is spread into many cells around its impact point. The ERIC algorithm constructs a nonet of cells and for the energy reconstruction, only the energy information of these nonet cells is taken into account. Each of these nonet cells has a specific fraction of the incident electron candidate energy and a specific ratio of energy leakage into the hadronic compartment. A weighting-technique computes the energy only for accepted track candidates. This weighting-technique yields a set of predicted energies. The difference of the energy measurement and the energy predictions is expressed by the probability function of the quality factor χ^2 ($P(\chi^2)$). An electron candidate is defined to have a reconstructed energy:

$$E_{ERIC} \quad with \quad P\left(\chi^2\right) > 10^{-2}. \tag{21}$$

In addition the ERIC routines yields several error codes. In the case of a "good" electron candidate all error codes are zero.

The energy scale is evaluated from the analysis of test beam data which were collected for different beam energies at various impact points distributed over the cell surface. For these test beam data the same stream of ERIC routines are called. The energy distribution is then fitted with a Gaussian distribution in the intervall
$E_{testbeam} - \sigma < E_{ERIC} < E_{testbeam} + 2\sigma$. The results for 10, 20, 40 and 80 GeV test beam electrons are shown in the figures 13 to 16 and table 2.

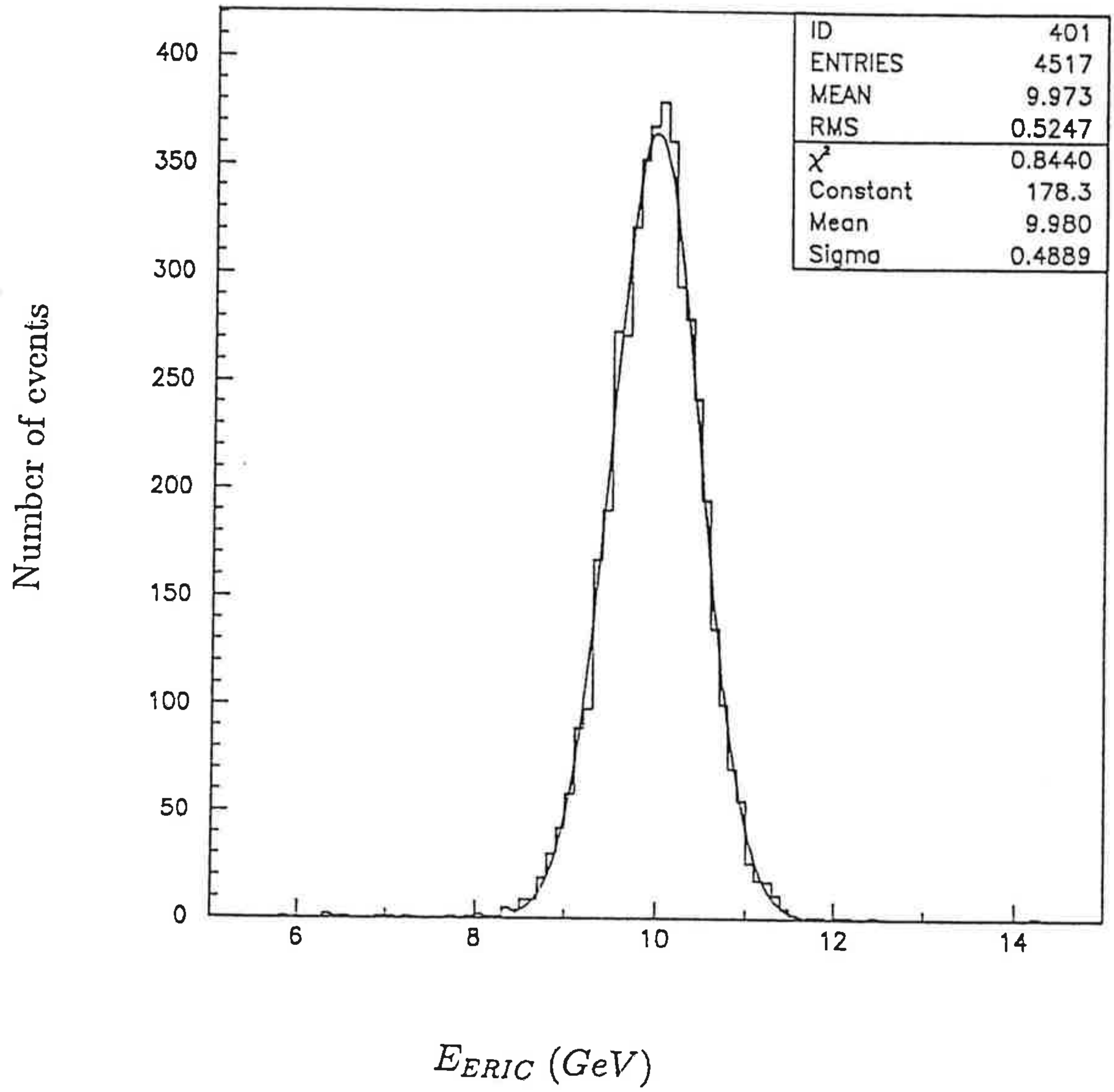

Figure 13: The energy response (ERIC) for 10 GeV test beam electrons together with a Gaussian fit.

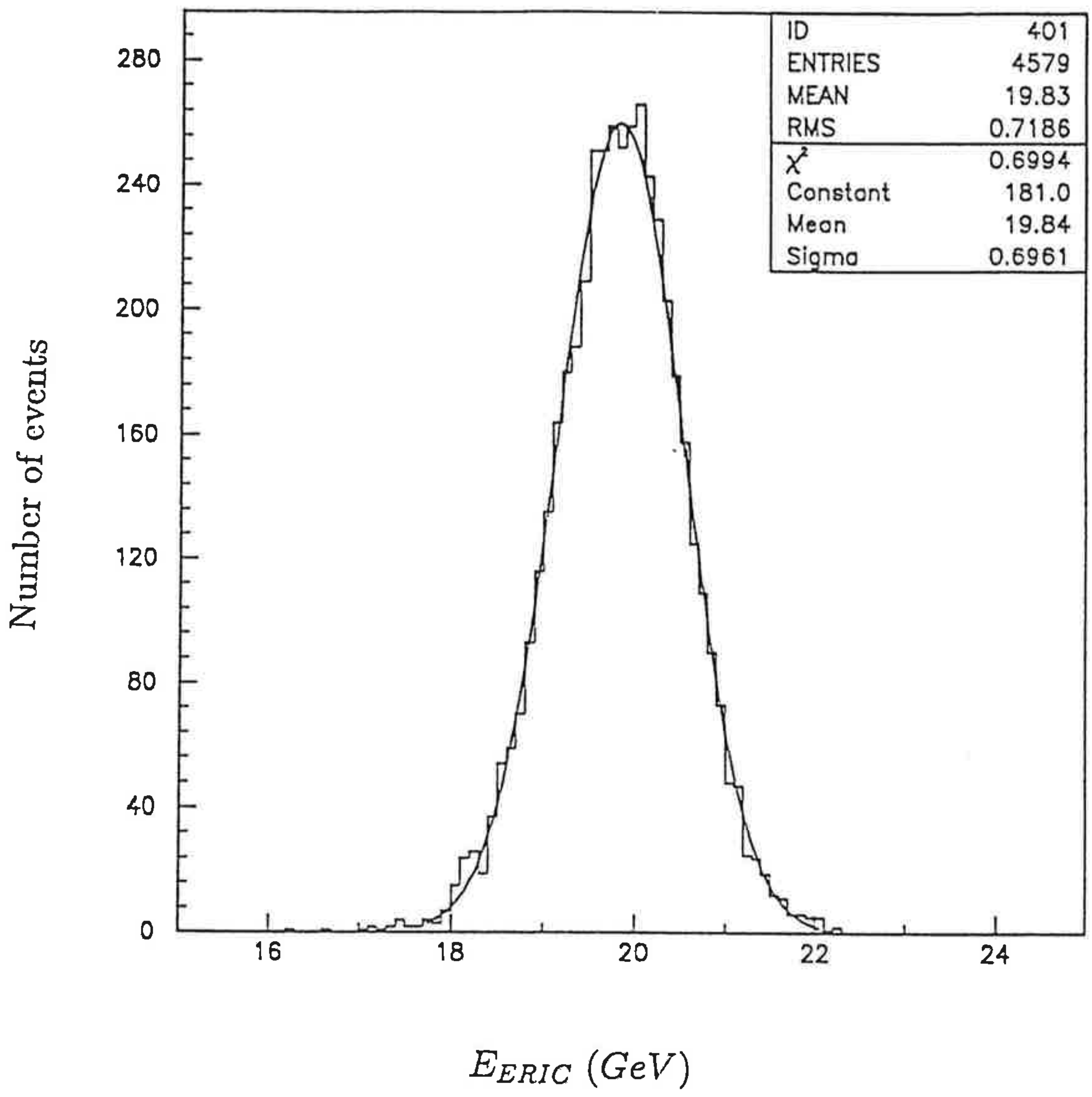

Figure 14: The energy response (ERIC) for 20 GeV test beam electrons together with a Gaussian fit.

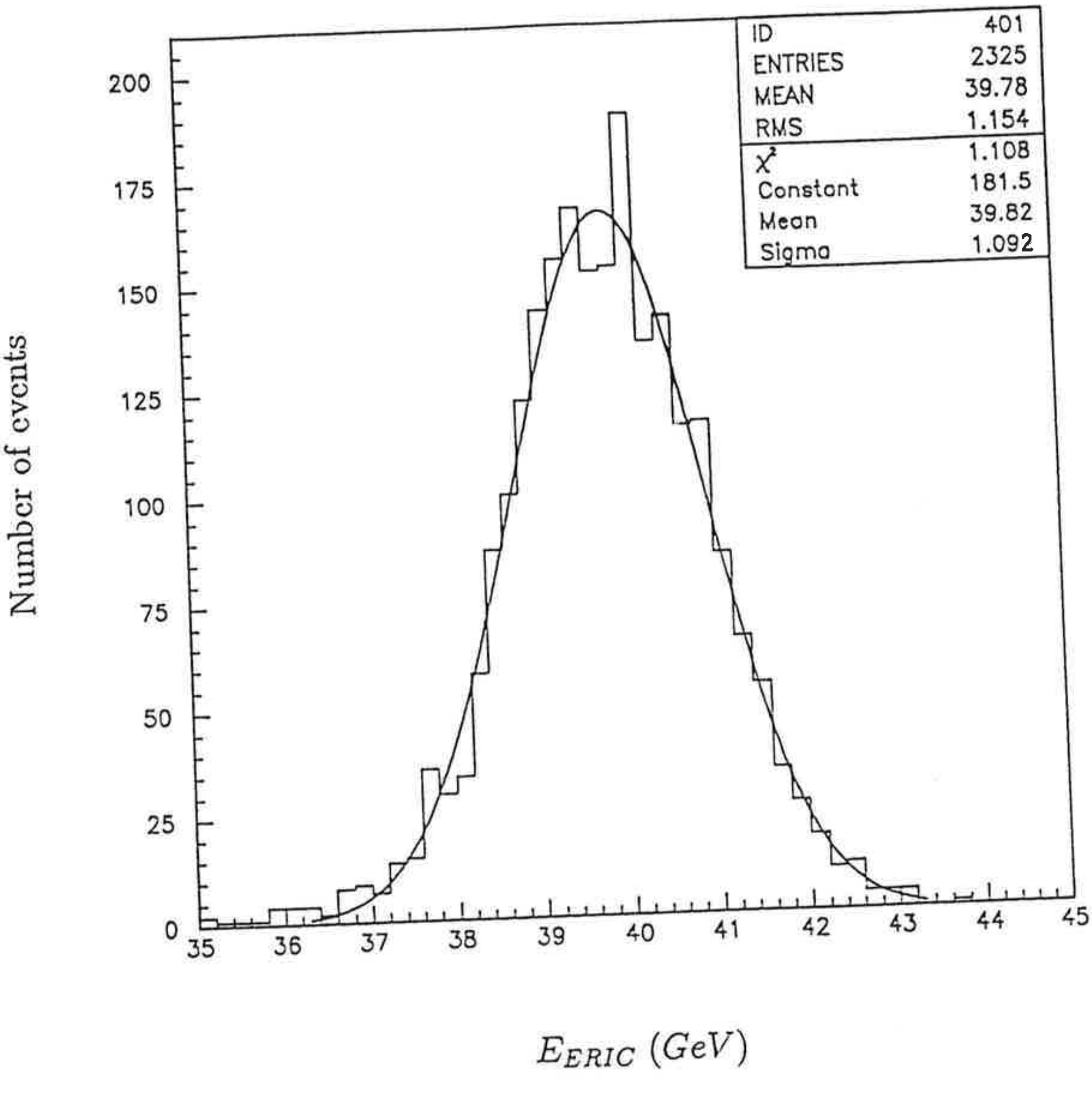

Figure 15: The energy response (ERIC) for 40 GeV test beam electrons together with a Gaussian fit.

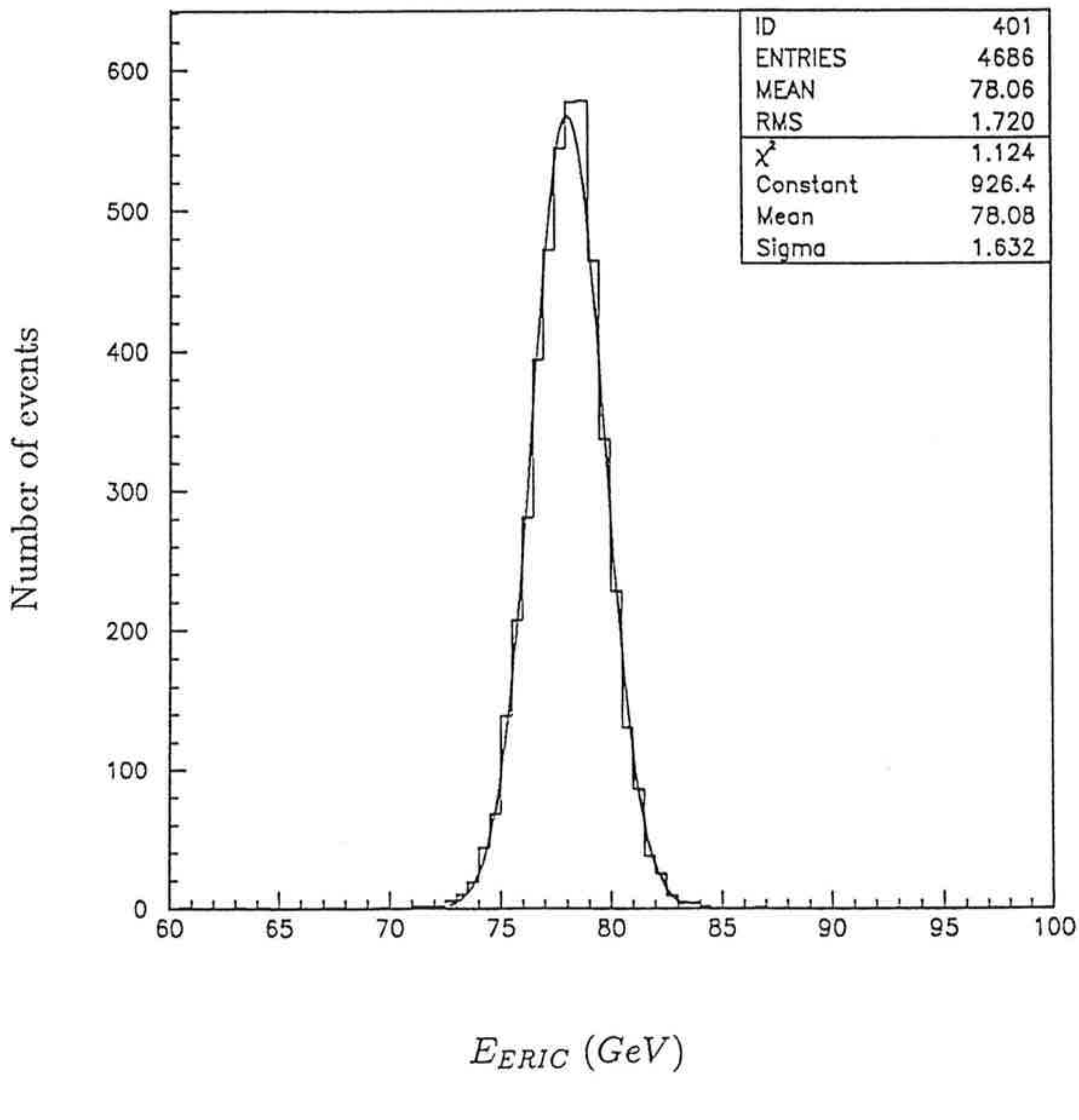

Figure 16: The energy response (ERIC) for 80 GeV test beam electrons together with a Gaussian fit.

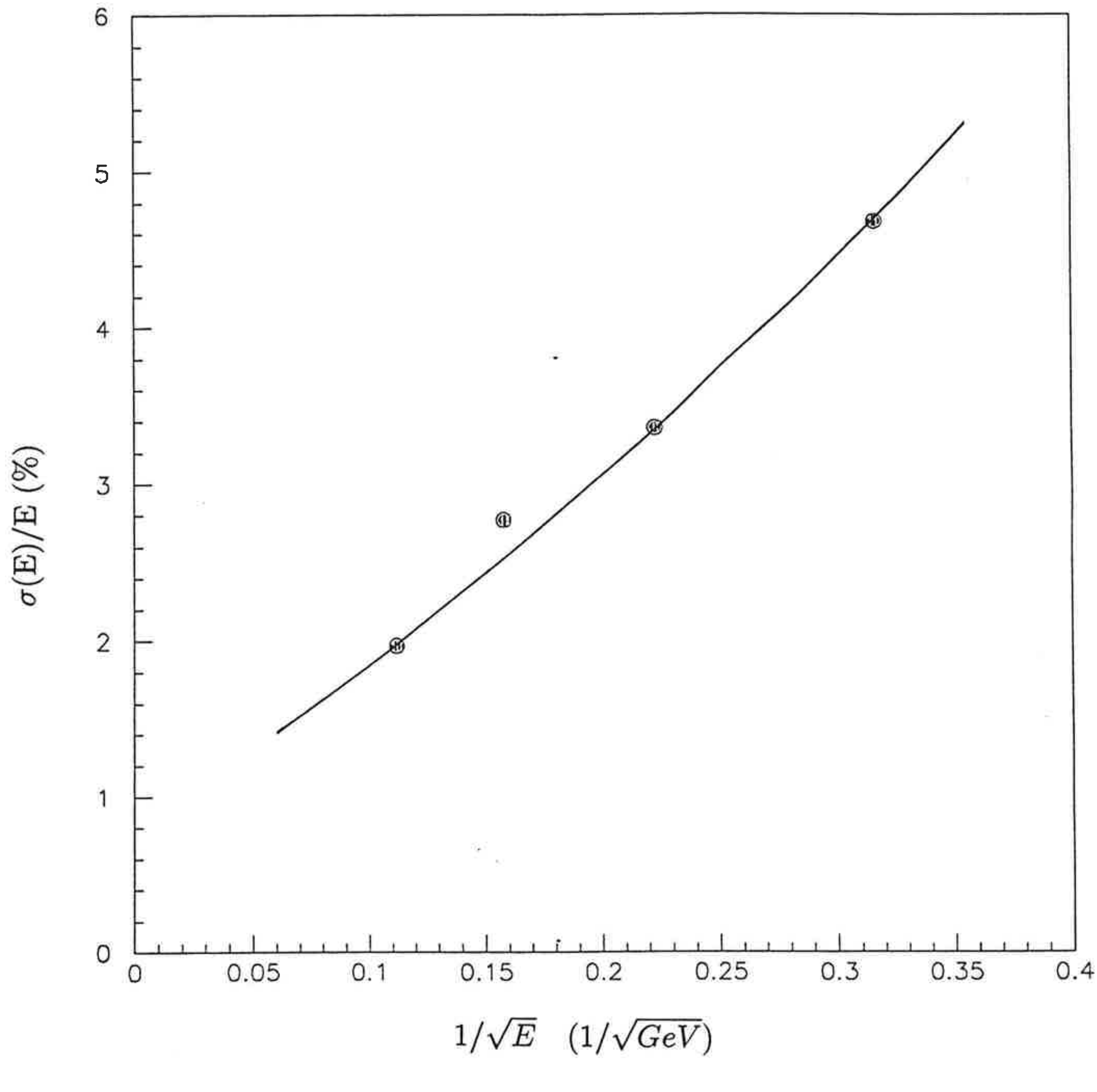

Figure 17: The energy resolution. These values are for electrons with impact points at the centre of the cell. The errors are not taken into account.

8 Calorimeter electron identification (CALELE) efficiency

The criterion to flag an electromagnetic cluster in terms of the hadronic leakage and shower radius is referred to as CALELE. Its efficiency depends on the "activity" of the underlying event and on the vertex offset. In order to study the CALELE efficiency we had to perform the analysis of test beam data for 10 *GeV* electrons. Test beam data are available for the different cell types (*central cells* or *edge cells*). The beam was scanned over the cell surface between $-5^0 < \theta < +5^0$ with the value of ϕ fixed at 0.0^0, and between $-7.5^0 < \phi < +7.5^0$ with the value of θ fixed at 0.0^0.

The effect of the underlying event activity was simulated by superimposing the energy pattern of minimum bias events to the electron test beam data. The values of the CALELE efficiencies are sensitive to the magnitude of the additional hadronic energy. In the data themselves, the magnitude of the underlying event is estimated by studying the $\Sigma\ E_T$ associated to that event, and by comparing it with the $\Sigma\ E_T$ obtained from a sample of minimum bias triggers. At present, we are still in the process of studying this in more detail, and we have used one minimum bias event for our preliminary numbers for the cross section calculation. Adding more than one minimum bias event would have a greater consequence for the efficiency of the *edge cells* than for *central cells* . We would like to note that $\approx$ 30 % of the events have one electron candidate in *edge cells* (1 and 10). The computation of the CALELE efficiency is summarized in the table below.

We note that the procedure is similar to that employed for the "W and Z analysis" [8], using incident electrons at 40 *GeV*. In particular we use the same scale factor, to account for the vertex offset (with respect to zero) in the calculation of the CALELE efficiency, at 10 *GeV* as was derived at 40 *GeV*. Furthermore, we have made consistency checks at an incident electron energy of 20 *GeV*.

Table 4: Results of the CALELE efficiency for 10 *GeV* electrons with one "minimum bias" event superimposed.

cell type	*efficiency* (in %)
central cells	87.3 ± 0.9
edge cells	74.9 ± 6.2

9 Selection criteria

9.1 Introduction

The large amount of data recorded in 1988 and 1989 had to be processed, and in our case only the events satisfiying the *"Z-trigger"* [8] bit were kept and written out on 32 Data Summary Tapes (DST's).

This data sample contains events with electron pair candidates produced in reactions as described in section 2. Therefore, a further selection procedure was applied in order to separate the signal from the background. In the following subsections the electron selection criteria are described.

9.2 Electron selection criteria

1. CLUSTERS.

   All events which contain two electromagnetic clusters (EM) in the central calorimeter are retained. An EM cluster fulfils the standard CALELE criteria:

   - the hadronic leakage should be consistent with the requirement:

   $$E_{H1}/E_{total} \; < \; 1.5 \; [0.023 \; + \; 0.035 \; ln \; (E_{total})] \, , \tag{23}$$

   - the cluster radius should be $R \; < \; 0.6$ cell units.

   Tracks within a cone of half-angle 15^0 from the event vertex facing the centre of gravity of the EM cluster are subjected to the electron selection criteria.

2. ERIC response.

   At least one track must exist inside the cone around the centre of gravity of the cluster. For this track the following ERIC reconstruction criteria must be satisfied:

   - ERROR code = 0 (*i.e.* normal completion code),
   - $P(\chi^2) > 10^{-2}$.

[8]Events with two electromagnnetic clusters (EM) separated in azimuth by $\Delta\phi \; \geq \; 60^0$.

3. SFD preshower match.

   The electron candidate is required to deposit a charge corresponding to 2 MIP per layer in the preshower part of the SFD detector. In addition the track of the electron candidate must match in (R,ϕ) (the plane perpendicular to the beam axis) and Z (along the beam direction) with the preshower position within the limits given by the corresponding resolutions:

   - $\sigma(\mathrm{R}\Delta\phi) = 0.4$ mm,
   - $\sigma(\mathrm{Z}) = 1.1$ mm.

   The quality of a track preshower match is defined by the variable:

$$d_\sigma^2 = \left[\frac{R\Delta\phi}{\sigma\,(R\Delta\phi)}\right]^2 + \left[\frac{\Delta Z}{\sigma\,(Z)}\right]^2, \tag{24}$$

   where $\Delta\phi$ and ΔZ correspond to the displacements between the track and preshower position. The electron candidate track is required to fulfil $\mathrm{d}_\sigma^2 < 25$.

These selection criteria are a necessary condition to select one track associated with an EM cluster. All the events analysed can be classified into three categories:

1. events with two EM clusters: $N_{ev}(EM - EM)$,
2. events with one electron candidate (global track with EM cluster satisfying the selection criteria) and further one EM cluster: $N_{ev}(EM - E)$,
3. events with two electron candidates: $N_{ev}(E - E)$.

9.3 Determination of efficiencies and rejections

The efficiencies and rejections of the detectors are determined by solving a set of quadratic equations that relate the observed number of events to the signal (S) and the background (B). The equations have the form:

$$N_{ij} = S\,(2\varepsilon_i\varepsilon_j - \varepsilon_j^2) + B\,(2\eta_i\eta_j - \eta_j^2), \tag{25}$$

where

- N_{ij} is the number of events which fulfil the selection criteria i and j. The criterion j includes the criterion i,
- $\varepsilon_{i,j}$ is the signal efficiency for the selection criterion used,
- $(\eta_{i,j})^{-1}$ is the rejection for the selection criterion used.

In practice, to solve these equations analytically is too complex, and one has to use numerical techniques. The MINUIT [25] program can be used to minimize the chisquare quantity χ^2. For the set of n equations, χ^2 is defined as

$$\chi^2 = \Sigma \left[\frac{\left[N_{ij} - S\left(2\varepsilon_i\varepsilon_j - \varepsilon_j^2\right) - B\left(2\eta_i\eta_j - \eta_j^2\right)\right]^2}{\sigma_{ij}^2} \right], \tag{26}$$

where σ_{ij}^2 is an estimate of the magnitude on the error of N_{ij}.

After applying the CALELE cuts to the data, the remaining data sample corresponds to $\sim$ 167k events in the mass interval 10 $GeV/c^2 < M_{ee} < 70\ GeV/c^2$.

This data sample is used for the evaluation of the efficiencies of the various cuts and selection criteria. First the technique used for the evaluation of the OSI and $SFD_{preshower}$ efficiencies is described; these efficiencies are then kept fixed in order to calculate the $ERIC$ and $SFD_{preshower}$ efficiencies.

9.4 SFD$_{preshower}$ and OSI pulse height cut efficiencies

In order to calculate the efficiency of the SFD$_{preshower}$ and the efficiency of the outer silicon pulse height cuts, a set of nine equations with seven unknowns are used. The $SFD_{preshower}$ efficiency is obtained from χ^2 as a function of the $SFD_{preshower}$ efficiency. The same procedure is applied to determine the OSI pulse height cut efficiency.

The error quoted for the $SFD_{preshower}$ efficiency is obtained from figure 18. The error quoted for the OSI pulse height cut efficiency is obtained from the figure 19 in the same way.

The fits yield:

$$\varepsilon_{SFD_{preshower}} = (80.2 \pm 3.8 \pm 2.0)\%, \tag{27}$$

$$\varepsilon_{OSI} = (70.0 \pm 2.3 \pm 2.0)\%. \tag{28}$$

The error quoted first is the statistical error, and the error quoted second is the systematic error obtained from the fit procedure.

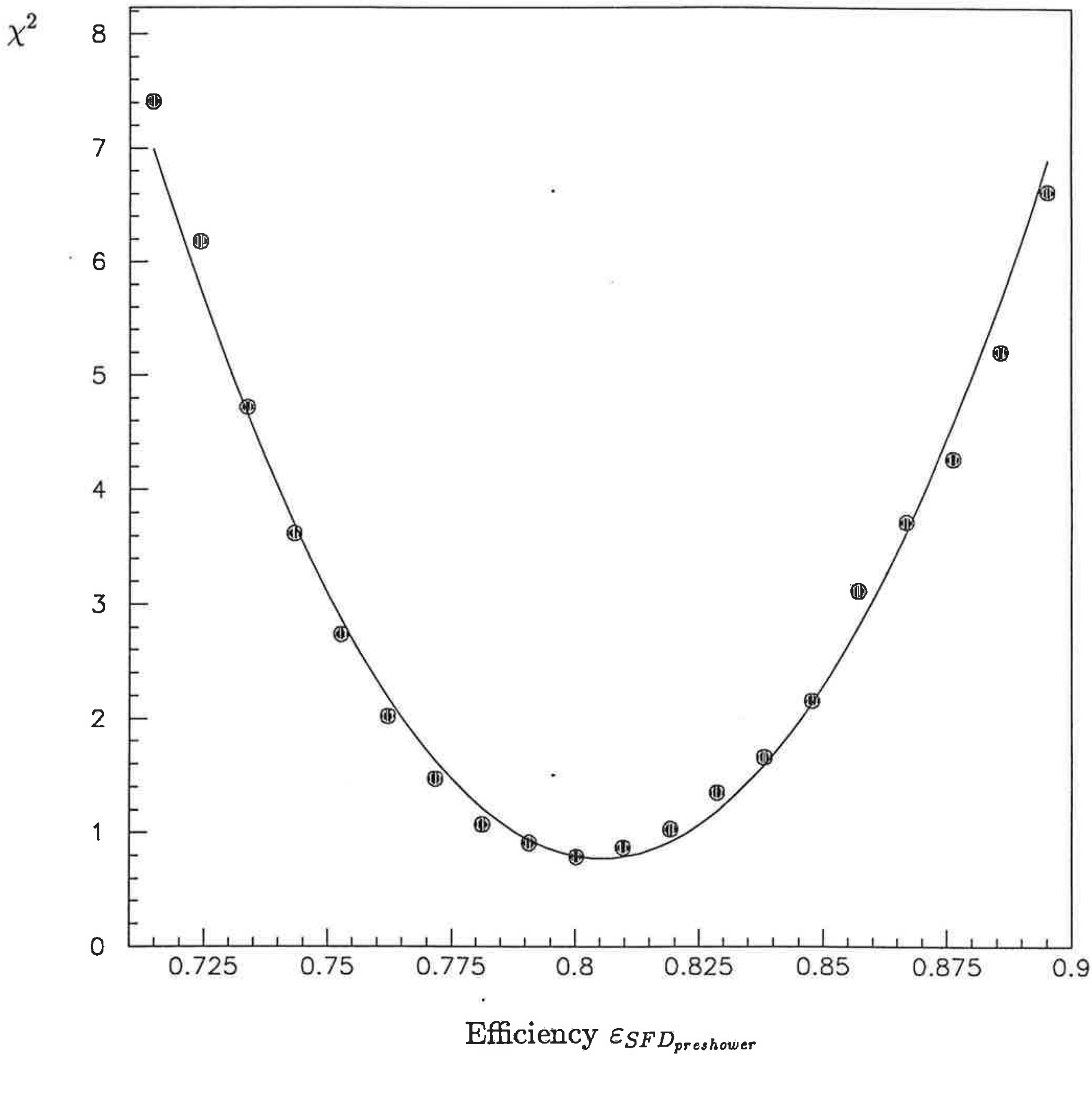

Figure 18: The evolution of χ^2 as a function of the SFD efficiency $\varepsilon_{SFD_{preshower}}$.

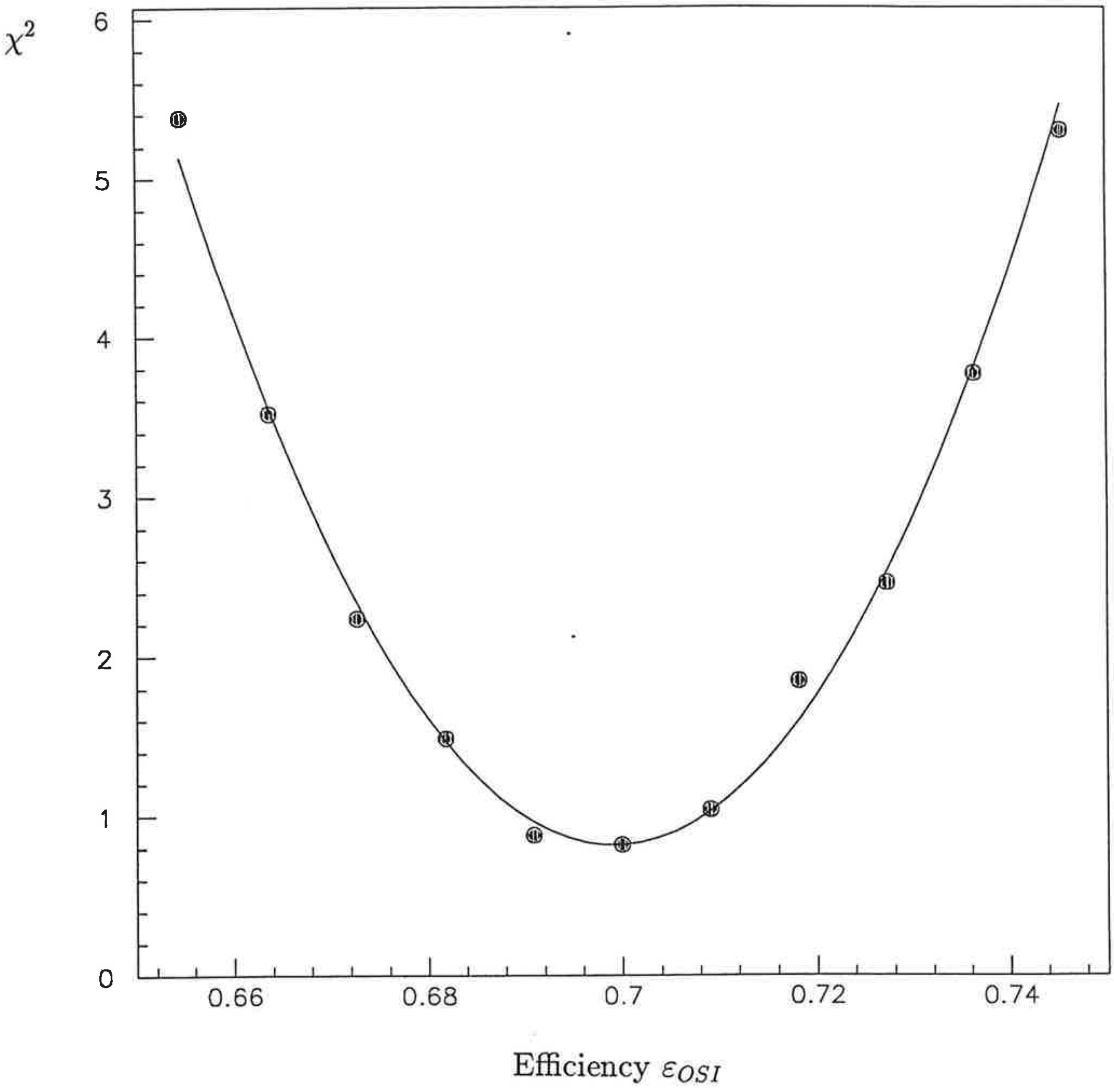

Figure 19: The evolution of χ^2 as a function of the OSI pulse height cut efficiency ε_{OSI}.

9.5 TRD and ERIC efficiencies

Having established the efficiencies of the $SFD_{preshower}$ and the OSI, these values are taken as input in the set of equations for the event sample summarized in table 5.

Table 5: Summary of the numbers of events obtained for the different selection criteria. These events are used for the calculation of the $ERIC$ and TRD efficiencies. $N_{ev}\,(E\ -\ E)$ refers to the number of events where both legs have passed the cuts.

Selection	$N_{ev}\,(E\ -\ E)$
Track-$SFD_{preshower}$	817
Track-$TRD_{charge\ cut}$	1021
Track-$ERIC_{P(\chi^2)\,10^{-2}}$	7786

The $TRD_{charge\ cut}$ efficiency is computed from the number of events (see table above) selected with the condition Track-ERIC compared to the number of events using the condition Track-TRD. The background events are subtracted. From the same selection criteria we also compute the TRD rejection factor against hadrons.

$$\varepsilon_{TRD} = (88.3 \pm 2.7)\,\%. \tag{29}$$

Likewise, the efficiency of the ERIC reconstruction criterion can be estimated. The ERIC efficiency is calculated for the requirement $P\,(\chi^2) > 10^{-2}$. To do this we remove the requirement of the ERIC response of the electron candidate track and instead apply the $SFD_{preshower}$ match cut. For clusters where more than one track matches the $SFD_{preshower}$ response the track with the smallest d_σ^2 is retained. The evaluation of the ERIC efficiency leads to the value

$$\varepsilon_{ERIC} = (90.2 \pm 2.6)\,\%. \tag{30}$$

The following table summarizes the results of the efficiency measurements.

Table 6: Summary of the efficiencies and rejections of the selection criteria. The ERIC efficiency is calculated using the condition $P(\chi^2) > 10^{-2}$.

Selection	*Efficiency* ε (in %)	*Rejection* $\sqrt{< R^2 >}$
ERIC	$90.2 \pm 2.6 \pm 1.3$	4.68
TRD	$88.3 \pm 2.7 \pm 0.3$	3.07
OSI	$70.0 \pm 2.3 \pm 2.0$	2.42
SFD	$80.2 \pm 3.8 \pm 2.0$	9.54

Note that

- the electron selection criteria are applied to the clusters and tracks in the sequential order given in table 6. The evaluation of the efficiencies and total rejections does not depend on this order, whereas the values of the separate rejections do,
- ε_{TRD} is obtained with fixed values of ε_{SFD} and ε_{OSI},
- ε_{ERIC} is obtained with fixed values of ε_{TRD} and ε_{OSI}.

The ERIC efficiency can also be determined with the requirement $P(\chi^2) > 10^{-4}$ as it is summarized in the following table. The determination of efficiencies and rejections for this case is done in the same way as described above.

Table 7: Summary of the efficiencies and rejections of the selection criteria. The ERIC efficiency is calculated using the condition $P(\chi^2) > 10^{-4}$.

Selection	*Efficiency* ε (in %)	*Rejection* $\sqrt{< R^2 >}$
ERIC	$95.1 \pm 1.8 \pm 1.6$	2.89
TRD	$87.9 \pm 2.6 \pm 0.3$	3.04
OSI	$70.0 \pm 2.3 \pm 2.0$	2.42
SFD	$80.2 \pm 3.8 \pm 2.0$	9.54

10 Final event selection

The above criteria applied to the data are sufficient for the determination of the various efficiencies. These selection criteria do not account for the E_t dependence of the trigger system for events with low E_t. In order to avoid threshold-effects, a further cut in E_t, is used instead of parametrizing the overall trigger efficiency.

The relevant selection criteria for the final data analysis are the following ones:

1. the event vertex within $-250\ mm < z_{vertex} < 250\ mm$,
2. two EM clusters passing the E_t cut,
3. a global track pointing to an EM cluster satisfying the standard CALELE criteria,
4. ERIC response with $P(\chi^2) > 10^{-2}$,
5. $SFD_{preshower}$ match with $d_\sigma^2 < 25$.

The following tables 8 and 9 summarize the number of events obtained by applying the above selection criteria to the data sample. For simplicity we abbreviate the selection criteria applied to both legs in the following way:

- TRK for an electron candidate associated with a global track,
- ERIC for an electron candidate associated with an ERIC response with $P(\chi^2) > 10^{-2}$,
- PS for an electron candidate associated with a $SFD_{preshower}$ response.

Table 8: Number of events obtained from different selection criteria in the invariant mass interval 10 $GeV/c^2 < M_{ee} < 70$ GeV/c^2 with the cut $E_t > 5.5$ GeV.

Selection	*Events*
(TRK-ERIC) · (TRK-ERIC)	583
(TRK-ERIC) · (TRK-ERIC-PS)	335
(TRK-ERIC-PS) · (TRK-ERIC-PS)	124

Table 9: Number of events obtained from different selection criteria in the invariant mass interval 10 $GeV/c^2 < M_{ee} < 70$ GeV/c^2 with the cut $E_t > 6.0$ GeV.

Selection	*Events*
(TRK-ERIC) · (TRK-ERIC)	394
(TRK-ERIC) · (TRK-ERIC-PS)	239
(TRK-ERIC-PS) · (TRK-ERIC-PS)	101

Table 10 contains the numbers of events selected in the different invariant mass regions.

Table 10: Number of events selected according to (TRK-ERIC-PS) · (TRK-ERIC-PS) in different invariant mass intervals for the E_t cuts.

Selection	$E_t > 5.5\ GeV$	$E_t > 6.0\ GeV$
$10\ GeV/c^2 < M_{ee} < 70\ GeV/c^2$	124	101
$10\ GeV/c^2 < M_{ee} < 14\ GeV/c^2$	24	15
$14\ GeV/c^2 < M_{ee} < 26\ GeV/c^2$	69	55
$26\ GeV/c^2 < M_{ee} < 50\ GeV/c^2$	24	24
$50\ GeV/c^2 < M_{ee} < 70\ GeV/c^2$	7	7

To take into account the different CALELE efficiencies for the two calorimeter cell types *central cell* and *edge cell* , we subdivide the event sample into the following categories: *central cell-central cell* , *edge cell-central cell* or *vice versa* and *edge cell-edge cell* .

Table 11: Number of events with electron candidates falling into the categories *CC-CC* , *EC-CC or CC-EC* and *EC-EC* .

Selection	$E_t > 5.5\ GeV$	$E_t > 6.0\ GeV$
$10\ GeV/c^2 < M_{ee} < 70\ GeV/c^2$	124	101
central cell-central cell (CC-CC)	88	73
EC-CC or CC-EC	34	28
edge cell-edge cell (EC-EC)	2	0

This distinction is also made for the geometrical acceptance.

10.1 Evaluation of signal and background

The determination of the QCD background can be performed using the MINUIT fitting technique as described above. As input parameter only the $SFD_{preshower}$ efficiency is used. The fit procedure yields a fitted signal S_{fit} and a rejection R_{fit}. These fit results and the number of events $N_{(TRK-ERIC)\cdot(TRK-ERIC)}$, the minimal selection criteria (TRK-ERIC) $\cdot$ (TRK-ERIC) as reported in table 8, are the ingredients to estimate the background:

$$background = \frac{N_{(TRK-ERIC)\cdot(TRK-ERIC)} - S_{fit}}{R_{fit}^2}. \quad (31)$$

Table 12: Number of signal and background events from the MINUIT fit as a function of the invariant mass with the cut $E_t > 5.5\, GeV$.

invariant mass	*fitted signal*	*rejection*	background	signal
$10\, GeV/c^2 < M_{ee} < 70\, GeV/c^2$	150.6	3.97	27.4	96.6
$10\, GeV/c^2 < M_{ee} < 14\, GeV/c^2$	23.6	3.85	8.9	15.1
$14\, GeV/c^2 < M_{ee} < 26\, GeV/c^2$	83.5	4.13	15.4	53.6
$26\, GeV/c^2 < M_{ee} < 50\, GeV/c^2$	30.4	2.93	4.5	19.5
$50\, GeV/c^2 < M_{ee} < 70\, GeV/c^2$	10.3	4.49	0.1	6.8

Table 13: Number of signal and background events from the MINUIT fit as a function of the invariant mass with the cut $E_t > 6.0\, GeV$.

invariant mass	*fitted signal*	*rejection*	background	signal
$10\, GeV/c^2 < M_{ee} < 70\, GeV/c^2$	132.7	4.13	15.3	85.7
$10\, GeV/c^2 < M_{ee} < 14\, GeV/c^2$	21.0	5.22	1.5	13.5
$14\, GeV/c^2 < M_{ee} < 26\, GeV/c^2$	67.5	3.99	11.6	43.4
$26\, GeV/c^2 < M_{ee} < 50\, GeV/c^2$	32.2	3.26	3.3	20.7
$50\, GeV/c^2 < M_{ee} < 70\, GeV/c^2$	10.3	4.49	0.1	6.8

The number of events (signal) after background subtraction listed in tables 12 and 13 are still contaminated with the background contribution from the semileptonic decay of $b\bar{b}$. The determination of this background contribution is estimated using the "PYTHIA" Monte Carlo simulation.

11 Monte Carlo Simulation

11.1 Introduction

The electron pair production in $p\bar{p}$ collision was simulated for the following reasons:

1. it allows to determine the geometrical acceptance of the UA2 apparatus.
2. it allows to estimate the $b\bar{b}$ background in the events sample.

For this purpose the Monte Carlo program "PYTHIA"[15] was used. The main features of this program are described in the following sections.

11.2 PYTHIA Monte Carlo generator

The generation of Drell-Yan events using the PYTHIA generator is performed according to the cross section for the subprocess:

$$q_i\bar{q}_i \longrightarrow \gamma^*/Z^0. \tag{32}$$

This cross section is calculated up to the first order in α_s, and the quarks are treated as massless. The electroweak coupling is expressed in term of α_{em}, M_Z, M_W and $sin^2\theta_W = 0.229$.

The proton and antiproton structure functions used, correspond to the parametrization proposed by Eichten et al. (EHLQ) [26]. The effects from initial and final state gluon radiation are also included. A detailed description of the PYTHIA program can be found in references [15] and [16].

The program is structured in the following way:

- initialisation:

  this part contains all the input parameters like the beam particles, the centre of mass energy and the value of the minimum transverse momentum of the central hard parton-parton scattering,
- generation of the user-chosen number of events,
- output:

  the calculation of the cross section.

For the generation of Drell-Yan events the following parameters were selected:

1. $p\bar{p}$ collision at the centre of mass energy $\sqrt{s} = 630\ GeV$,
2. minimum transverse momentum of the central hard parton-parton scattering, $Q_{t_{min}} = 0.0\ GeV/c$,

3. minimum invariant mass of the electron pairs, $M_{min} = 10.0\ GeV/c^2$,

4. K-factor, $K = 1.65$,

5. process at parton level:

$$\begin{array}{llllll} & q\bar{q} & \longrightarrow & \gamma^*/Z^0 & \longrightarrow & e^+e^- \\ (i.e. & p\bar{p} & \longrightarrow & e^+e^- & + & X). \end{array} \tag{33}$$

The events, distributed over 4π, are generated with the vertex point at (0,0,0). The interface between the simulated events and UA2 detector is provided by a particle bank called PAMM, where the generated quantities (i.e. P_x, P_y, P_z, E) are stored. For each event a set of PAMM-banks are produced.

In order to calculate the geometrical acceptance of the UA2 detector for the Drell-Yan electron pairs, one has to check for each event that the two electrons originate from the γ^*/Z^0 propagator, and not from background processes (e.g. Dalitz decays).

11.3 Generated events in the UA2 detector

The generated events have to be tracked through the UA2 detector. For this purpose a set of routines, stored under MCRUN, are called with the aim:

- to smear the vertex according to the observed distribution in $p\bar{p}$ collisions (Gaussian distribution with an $r.m.s = 109$ mm),
- to create banks for each detector present between the vertex and the calorimeter cell,
- to create a track bank TKMM which contains the information of all the track segments measured.

11.4 Determination of the geometrical acceptance

The geometrical acceptance of the UA2 detector for electron pairs is defined by the requirement, that both electrons have to satisfy the same geometrical cuts as in the data themselves. Restricting ourselves to the central part of the UA2 detector,

1. both electrons have to hit the central calorimeter inside the active [9] volume [1],
2. both electrons have to pass through the $SFD_{preshower}$ and $SFD_{tracking}$ detectors,
3. both electrons have to traverse the active volume (pad) of the outer silicon detector OSI,
4. both electrons have to be in the active volume of the inner silicon detector ISI.

[9] The active volume is given by the cell size.

11.5 Results for the acceptance calculation

The geometrical acceptance is computed as a function of the invariant mass M_{ee}.

In order to take into account the trigger conditions, the azimuthal angle between the electron tracks must be $\Delta\phi > 60^0$.

Furthermore, the energy of each electron is smeared according to a Gaussian resolution function, where the parameters are indicated in table 3. (section 7).

The geometrical acceptance η is defined by

$$\eta = \frac{N_{acc}}{N_{Generated}}, \tag{34}$$

where

N_{acc} is the number of events in the central calorimeter.

$N_{Generated}$ is the total number of generated events.

11.6 Geometrical acceptance as a function of the invariant mass

In the following, the geometrical acceptance of the central part of the UA2 detector is computed as a function of the invariant mass M_{ee} for the two cuts in E_t in the same way as it was done for the data selection (see section 7.).

The effect of the energy smearing is taken into account (as obtained from the determination of the energy resolution). Tables 14 to 16 summarize the acceptances found.

The number of events in a specific invariant mass region is used as "normalisation" factor for the computation of the acceptance.

Table 14: The geometrical acceptance (the effect of energy smearing is taken into account), as a function of the invariant mass interval for $E_t > 5.5\ GeV$.

invariant mass	*acceptance* η (in %)
$10\ GeV/c^2 < M_{ee} < 70\ GeV/c^2$	11.59 ± 0.09
$10\ GeV/c^2 < M_{ee} < 14\ GeV/c^2$	3.08 ± 0.08
$14\ GeV/c^2 < M_{ee} < 26\ GeV/c^2$	15.02 ± 0.16
$26\ GeV/c^2 < M_{ee} < 50\ GeV/c^2$	20.91 ± 0.28
$50\ GeV/c^2 < M_{ee} < 70\ GeV/c^2$	27.31 ± 0.82

Table 15: The geometrical acceptance (the effect of energy smearing is taken into account), as a function of the invariant mass region for $E_t > 6.0\ GeV$.

invariant mass	*acceptance* η (in %)
$10\ GeV/c^2 < M_{ee} < 70\ GeV/c^2$	10.58 ± 0.09
$10\ GeV/c^2 < M_{ee} < 14\ GeV/c^2$	1.43 ± 0.05
$14\ GeV/c^2 < M_{ee} < 26\ GeV/c^2$	14.13 ± 0.16
$26\ GeV/c^2 < M_{ee} < 50\ GeV/c^2$	20.90 ± 0.28
$50\ GeV/c^2 < M_{ee} < 70\ GeV/c^2$	27.31 ± 0.82

The evaluation of the acceptance for the different categories : *central cell-central cell* , *edge cell-central cell* or *vice versa* and *edge cell-edge cell* leads to the numbers shown in table 16.

Table 16: The acceptance for electron candidates falling into the categories *CC-CC* , *EC-CC* or *CC-EC* and *EC-EC* .

Selection	$E_t > 5.5\ GeV$ (in %)	$E_t > 6.0\ GeV$ (in %)
$10\ GeV/c^2 < M_{ee} < 70\ GeV/c^2$	11.59	10.58
central cell-central cell (CC-CC)	7.10	6.46
EC-CC or CC-EC	3.96	3.64
edge cell-edge cell (EC-EC)	0.52	0.48

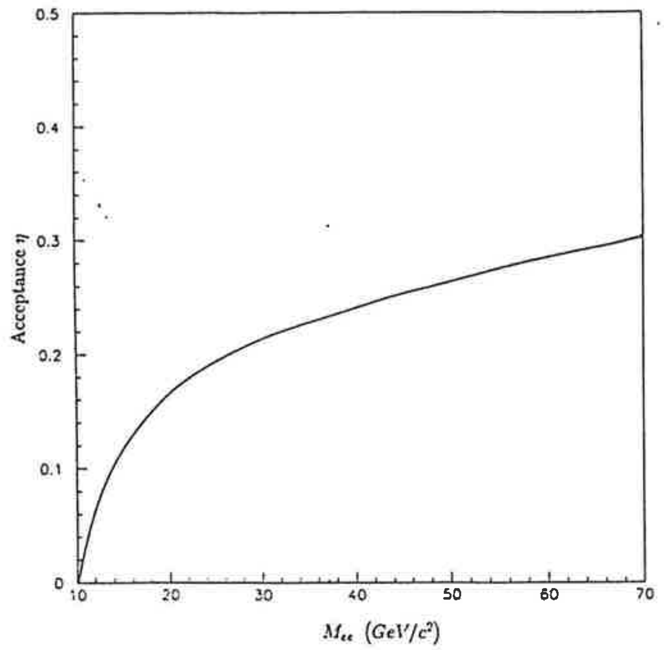

Figure 20: Acceptance versus the invariant mass with $E_t > 5.5\ GeV$.

Figure 21: Acceptance versus the invariant mass with $E_t > 6.0\ GeV$.

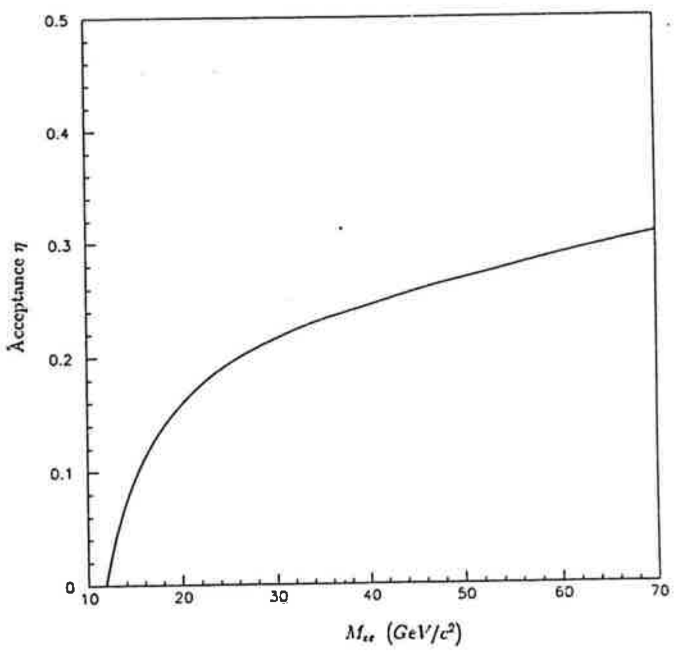

11.7 Evaluation of the $b\bar{b}$ background

The production of $b\bar{b}$ in hadron hadron collision with the subsequent semileptonic decay of both *b's* into electrons, neutrinos and a pair of *charm* quarks (or quarks lighter than the charm quark) is a source of background to the Drell-Yan electron pair production, because of its high production cross section of $\mathcal{O}(10\ \mu b)$. The signature of the double semielectronic decay of $b\bar{b}$ is similar to the signature for the Drell-Yan electron pair production. The main difference in the two reactions lies in the fact, that the *jets* produced in the semileptonic decay of the *b's* accompany the electrons, whereas the *jets* , eventually produced together with the Drell-Yan electron pair, normally do not. Therefore, the electrons from the Drell-Yan electron pair production are isolated.

11.7.1 Generation of $b\bar{b}$ events

The PYTHIA generator, to generate $b\bar{b}$ events, is used with the following parameters:

1. $p\bar{p}$ collision at the centre of mass energy $\sqrt{s}\ =\ 630\ GeV$,
2. minimum transverse momentum of the central hard parton-parton scattering $Q_{t_{min}}\ =\ 5.0\ GeV/c$,
3. process at parton level:

$$g + g \longrightarrow b + \bar{b}. \tag{35}$$

The number of $b\bar{b}$ events generated has to be "normalized" to the integrated luminosity of the experiment. For this purpose the $b\bar{b}$ production cross section for the cut $q_t^b\ >\ 5.0\ GeV$, obtained from the method described by Nason et al. [21], is used.

$$\sigma\left(p\bar{p}\ \rightarrow\ b\bar{b}\ +\ X\ ;\ q_t^b\ >\ 5.0\ GeV\right)\ =\ 3.99\ ^{+2.04}_{-1.47}\ \mu b. \tag{36}$$

This cross section is compatible with the $b\bar{b}$ production cross section, evaluated by UA1 [22]. Assuming this value for the $b\bar{b}$ production cross section, the $\approx$ 54k generated events correspond to an integrated luminosity of 13.5 nb^{-1}.

11.7.2 Simulation of the central calorimeter

Similarly to the computation of the geometrical acceptance for Drell-Yan electron pairs, also the electrons from $b\bar{b}$ had to be processed with the same geometrical cuts (see previous section).

The events are selected in the invariant mass region of $10\ GeV/c^2\ <\ M_{ee}\ <\ 70\ GeV/c^2$. The resulting event samples in function of the E_t cut are summarized in the following table:

Table 17: The $b\bar{b} \rightarrow eeX$ events, satisfying the geometrical cuts, versus the E_t cut.

E_t *cut*	N_{event}
$E_t > 5.5\ GeV$	27
$E_t > 6.0\ GeV$	20

In order to calculate the CALELE and ERIC efficiencies for electrons with jet activity, the central calorimeter was fully simulated. For this purpose, a model exists which takes into account the sharing of the photomultiplier response of one cell produced by electrons (from the $W^{\pm}$ decay) accompanied by *jets* .

The results of the CALELE and ERIC efficiency calculation as a function of the E_t cut are given in the following tables.

Table 18: The efficiencies for the CALELE condition applied to the electrons from $b\bar{b}$ as a function of the E_t cut.

E_t *cut*	*CALELE efficiency* (in %)
$E_t > 5.5\ GeV$	41.87 ± 1.9
$E_t > 6.0\ GeV$	38.79 ± 2.3

Table 19: The efficiencies for ERIC under the condition $P(\chi^2) > 10^{-2}$ applied to the electrons from $b\bar{b}$ as a function of the E_t cut.

E_t *cut*	*ERIC efficiency* (in %)
$E_t > 5.5\ GeV$	60.14 ± 1.9
$E_t > 6.0\ GeV$	55.11 ± 2.3

11.7.3 Numbers of $b\bar{b}$ background events

The evaluation of the number of $b\bar{b}$ background events is performed using the following relation:

$$n_{b\bar{b}} = \frac{N_{acc}}{N_{gen}} \cdot \mathcal{L} \cdot \sigma_{b\bar{b}} \cdot \left(BR \cdot \varepsilon_{tracking} \cdot \varepsilon_{preshower} \cdot \varepsilon_{calele} \cdot \varepsilon_{eric}\right)^2 , \quad (37)$$

where:

N_{acc} are the numbers of accepted $b\bar{b}$ events in the central calorimeter,
N_{gen} are the numbers of generated $b\bar{b}$ events,
$\mathcal{L}$ is the integrated luminosity,
$\sigma_{b\bar{b}}$ is the cross section for the $b\bar{b}$ production (with $q_t^b > 5.0\ GeV$) and
BR is the branching ratio for the semielectronic decay of a *B-meson* (BR = 12.3 %).

Taking all these numbers into account, the computed numbers of $b\bar{b}$ background events in the central calorimeter in function of the E_t cut are summarized in table 20.

Table 20: The numbers of $b\bar{b}$ background events in the central calorimeter as a function of the E_t cut.

E_t *cut*	$N_{b\bar{b}}$
$E_t > 5.5\ GeV$	7.5 ± 3.7
$E_t > 6.0\ GeV$	4.0 ± 2.0

The large errors are due to the uncertainty in the cross section for the $b\bar{b}$ production.

The numbers of $b\bar{b}$ events in the different invariant mass intervals and for the two E_t cuts can be found in the next table.

Table 21: Numbers of $b\bar{b}$ background events (BG) in the different invariant mass interval and for the two E_t cuts.

invariant mass	background events for $E_t > 5.5\ GeV$	background events $E_t > 6.0\ GeV$
$10\ GeV/c^2 < M_{ee} < 70\ GeV/c^2$	7.5	4.0
$10\ GeV/c^2 < M_{ee} < 14\ GeV/c^2$	2.0	0.4
$14\ GeV/c^2 < M_{ee} < 26\ GeV/c^2$	5.0	3.2
$26\ GeV/c^2 < M_{ee} < 50\ GeV/c^2$	0.5	0.4
$50\ GeV/c^2 < M_{ee} < 70\ GeV/c^2$	0.0	0.0

In figures 22 and 23 the distribution of the data for the invariant mass intervals
$10\ GeV/c^2 < M_{ee} < 14\ GeV/c^2$,
$14\ GeV/c^2 < M_{ee} < 26\ GeV/c^2$,
$26\ GeV/c^2 < M_{ee} < 50\ GeV/c^2$,
$50\ GeV/c^2 < M_{ee} < 70\ GeV/c^2$,

is shown for the cuts $E_t > 5.5\ GeV$ and $E_t > 6.0\ GeV$. The contribution of the QCD background is shown with the open circles and the contribution of the $b\bar{b}$ background is shown with the open triangles. The horizontal lines correspond to the bin widths.

Note that the points are put artificially into the middle of these bins. The drawn vertical error bars correspond to the statistical uncertainties.

Figures 24 and 25 show the distributions of the data , by applying the final selection criteria and subtracting the QCD and $b\bar{b}$ background, as function of the invariant mass. The energy-smeared Monte Carlo events (taking into account the energy resolution for electrons in *central cells* and for *edge cells*) are superimposed onto the data.

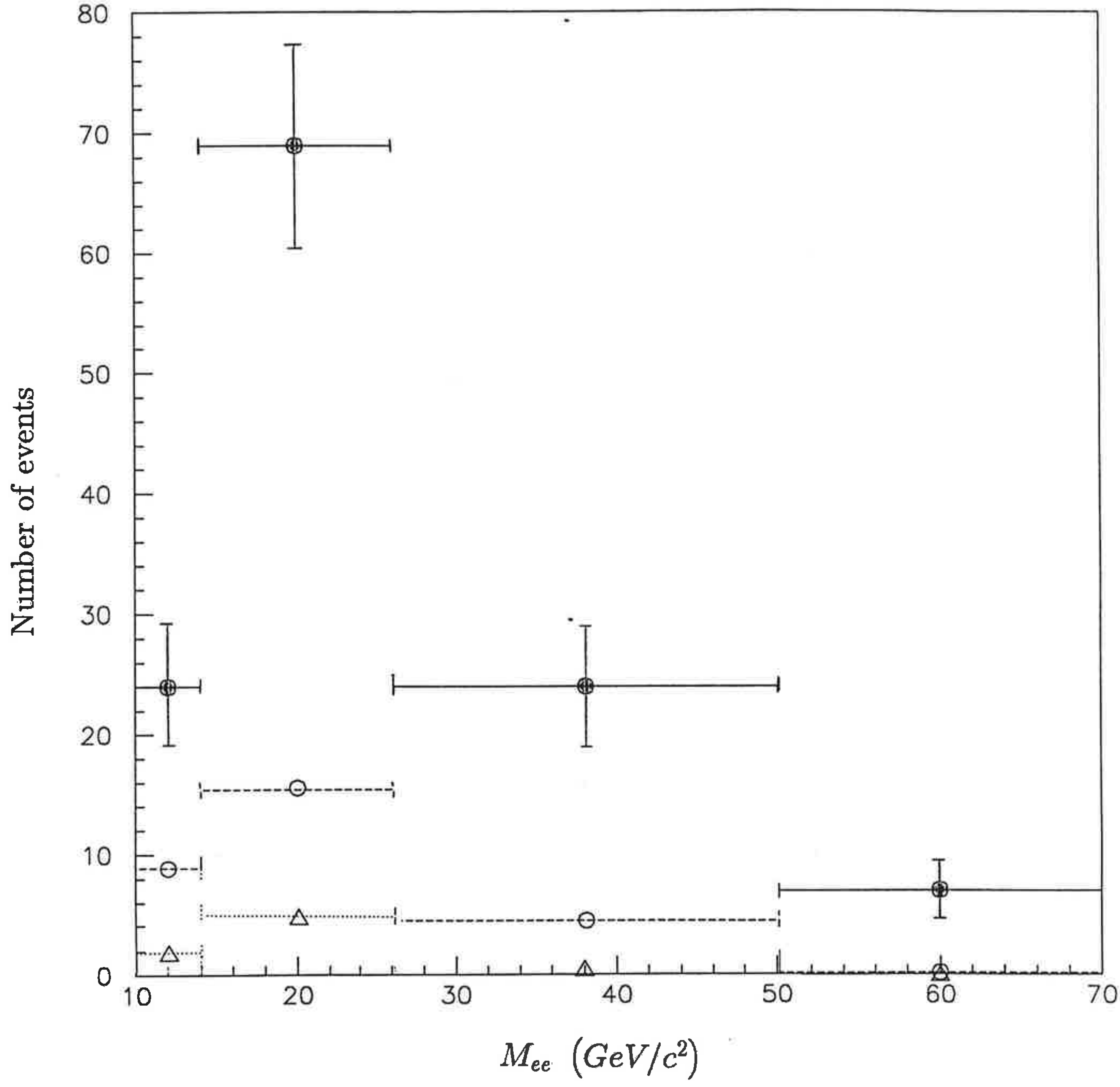

Figure 22: The distribution of the data in function of the invariant mass M_{ee} for $E_t > 5.5\ GeV$. The open circles represent the contribution of QCD background and the open triangles represent the contribution of $b\bar{b}$ background. The vertical bars correspond to the statistical errors and the horizonal lines correspond to the bin widths.

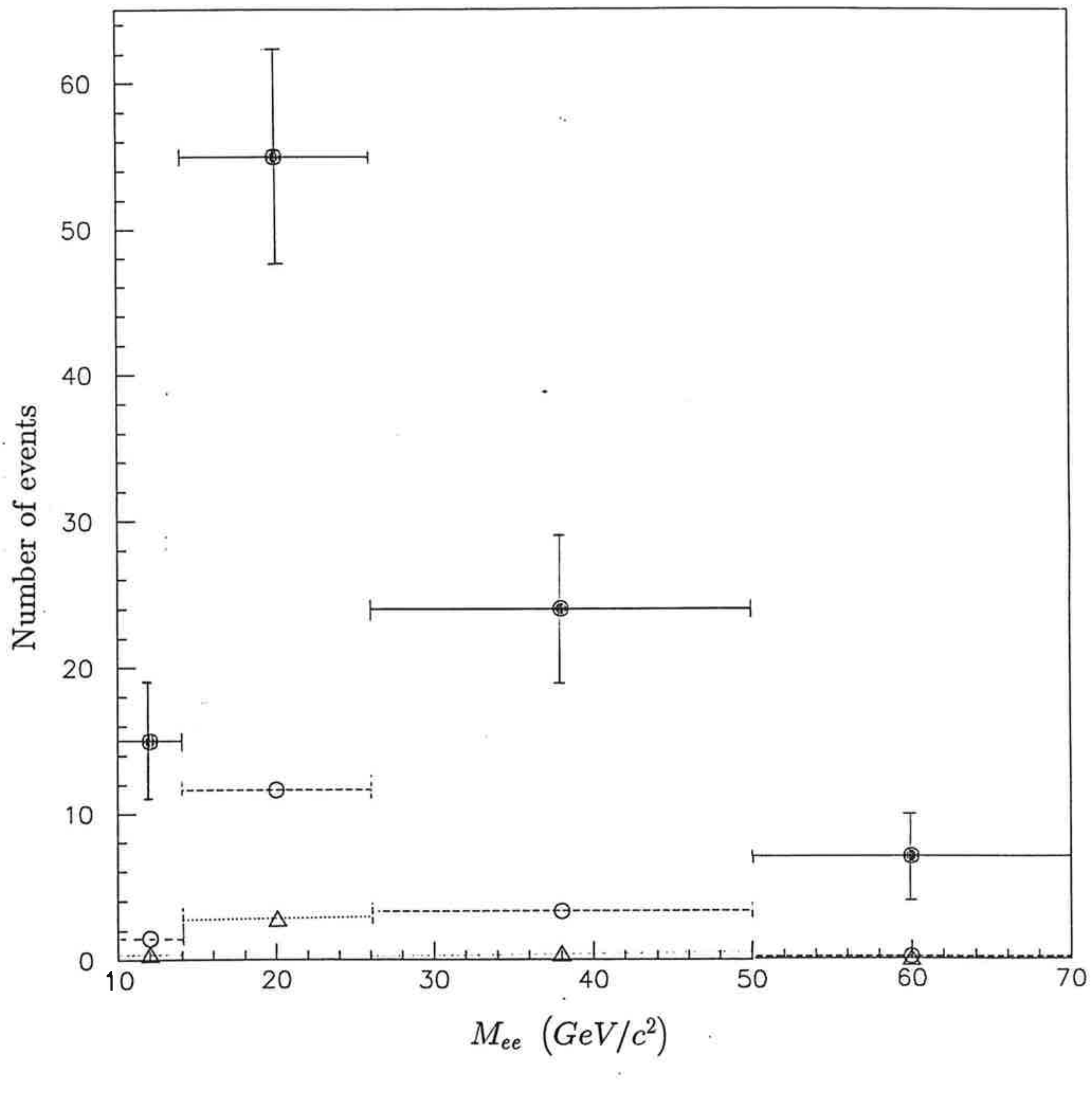

Figure 23: The distribution of the data in function of the invariant mass M_{ee} for $E_t > 6.0\ GeV$. The open circles represent the contribution of QCD background and the open triangles represent the contribution of $b\bar{b}$ background. The vertical bars correspond to the statistical errors and The horizonal lines correspond to the bin widths.

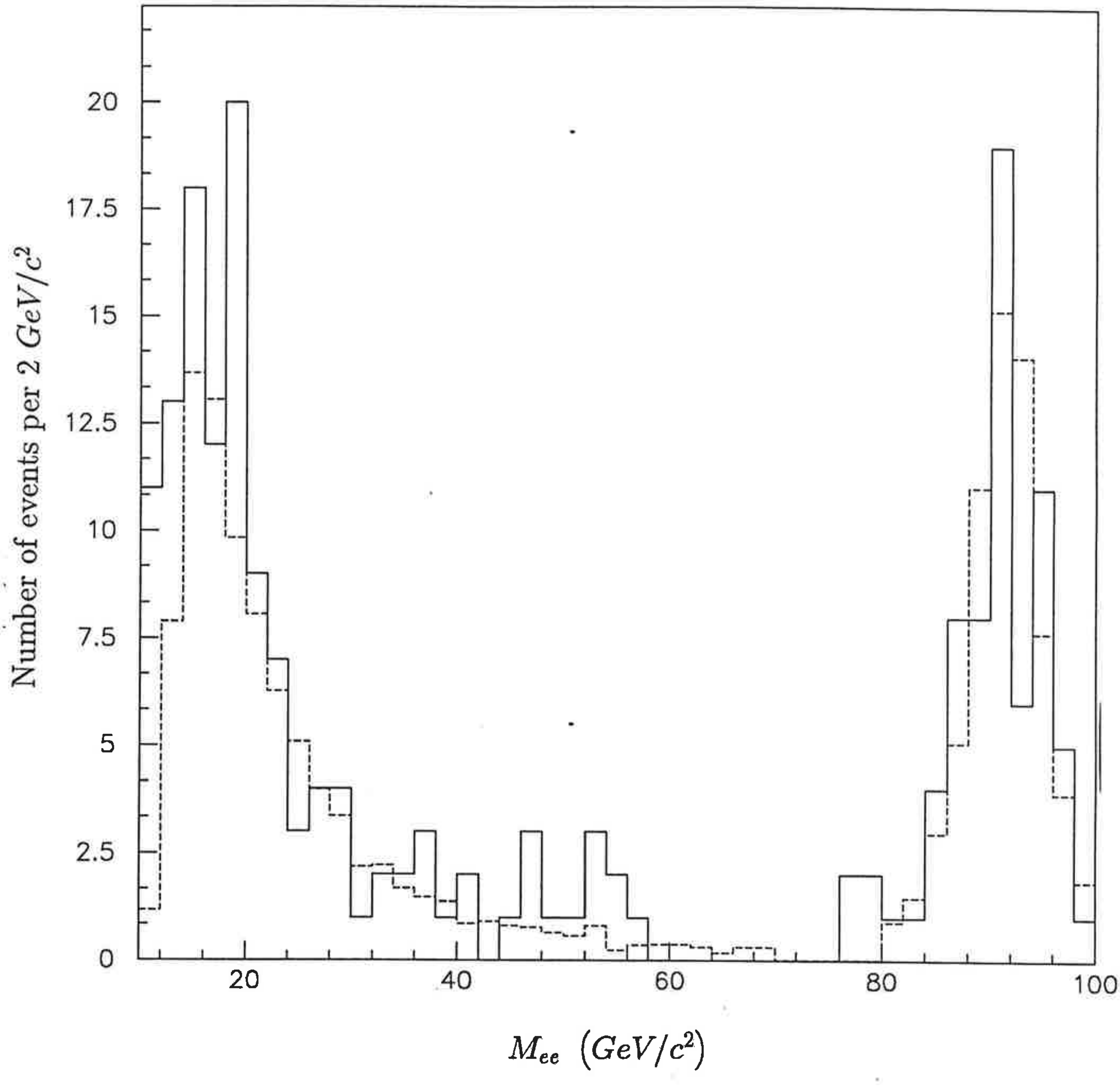

Figure 24: The distribution of the data (full curve) in the central calorimeter as a function of the invariant mass M_{ee} with $E_t > 5.5\,GeV$. Superimposed is the distribution of Monte Carlo events (dashed curve) with the energy resolution taken into account.

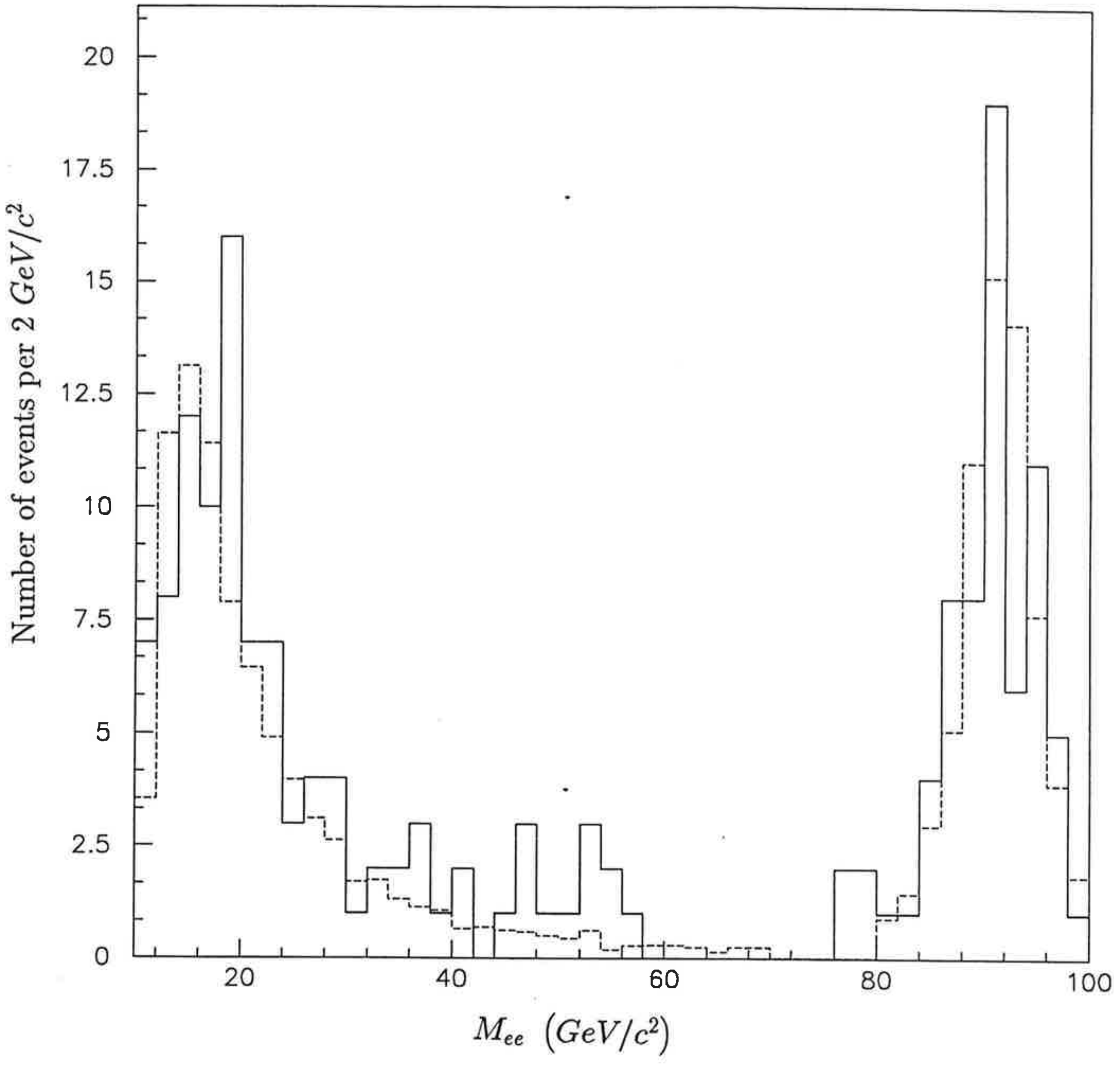

Figure 25: The distribution of the data (full curve) in the central calorimeter as a function of the invariant mass M_{ee} with $E_t > 6.0\ GeV$. Superimposed is the distribution of Monte Carlo events (dashed curve) with the energy resolution taken into account.

12 Cross section for the Drell-Yan electron pair production

The cross section for the Drell-Yan electron pair production in the invariant mass interval $10\ GeV/c^2 < M_{ee} < 70\ GeV/c^2$ is determined by:

$$\sigma_{DY} = \frac{S - BG_{QCD} - BG_{b\bar{b}}}{\mathcal{L} \cdot \eta \cdot \varepsilon^2}. \tag{38}$$

where

S are the numbers of events obtained by applying the final selection criteria, (summarized in tables 8 and 9 on page 43),

BG_{QCD} are the numbers of QCD background events, (summarized in tables 12 and 13 on pages 45 and 46),

$BG_{b\bar{b}}$ are the numbers of $b\bar{b}$ background events, (summarized in table 20 on page 20),

$\mathcal{L}$ is the integrated luminosity,

η is the acceptance (summarized in the following table):

Table 22: Summary of the acceptance values used for the calculation of the Drell-Yan cross section.

category	η for $E_t > 5.5\ GeV$ (in %)	η for $E_t > 6.0\ GeV$ (in %)
central cell - central cell	7.10 ± 0.09	6.46 ± 0.09
central cell-edge cell or *vice versa*	3.96 ± 0.09	3.64 ± 0.09

and ε is the product:

$$\varepsilon = \varepsilon_{vertex} \cdot \varepsilon_{tracking} \cdot \varepsilon_{SFD_{preshower}} \cdot \varepsilon_{ERIC} \cdot \varepsilon_{CALELE}.$$

Table 23: Summary of the efficiency values used for the calculation of the Drell-Yan cross section.

name	efficiency (in %)
ε_{vertex}	94.3 ± 0.5
$\varepsilon_{tracking}$	90.6 ± 1.1
$\varepsilon_{SFD_{preshower}}$	80.2 ± 4.3
ε_{ERIC}	90.2 ± 2.9
ε_{CALELE} *central cell*	87.3 ± 0.9
ε_{CALELE} *edge cell*	74.9 ± 6.2

We present values for the cross section for two E_t cuts, in order to check the consistency. Presently we have extrapolated the cross section to a lower value of the invariant mass M_{ee} at 10 GeV/c^2 using the Drell-Yan Monte Carlo calculation in both cases. We compute the cross section for the two categories: *central cell-central cell* and *edge cell-central cell* or *vice versa* . (We do not consider further the small number of events with electron candidates falling into the category *edge cell-edge cell* .) The cross sections for the two categories are labelled as follows:

- σ_1 for the category *central cell-central cell,*
- σ_2 for the category *edge cell-central cell* or *vice versa.*

Table 24: The cross sections with the statistical errors for the two categories *CC-CC* and *EC-CC or CC-EC* and for the two E_t cuts in the invariant mass interval $10\ GeV/c^2 < M_{ee} < 70\ GeV/c^2$.

category	$E_t > 5.5\ GeV$	$E_t > 6.0\ GeV$
σ_1	389 pb	400 pb
$\Delta\sigma_1$	65 pb	63 pb
σ_2	314 pb	317 pb
$\Delta\sigma_2$	85 pb	81 pb

The values in table 24 lead to the weighted average Drell-Yan cross section for electron pairs, produced through $p\bar{p}$ collisions at the centre of mass energy $\sqrt{s} = 630\ GeV$ in the invariant mass interval $10\ GeV/c^2 < M_{ee} < 70\ GeV/c^2$:

$$\bar{\sigma}\,(p\bar{p} \rightarrow e^+e^- + X\,) = (362 \pm 52\ (stat.)\ \pm 58\ (syst.)\ )\,pb$$

$$\bar{\sigma}\,(p\bar{p} \rightarrow e^+e^- + X\,) = (368 \pm 50\ (stat.)\ \pm 58\ (syst.)\ )\,pb$$

where the first value of the average cross section is for the data selected with the cut $E_t > 5.5\ GeV$ and the second one with the $E_t > 6.0\ GeV$ cut.

The systematic errors are estimated by propagating the individual uncertainties on the magnitude of the quantities used in the calculation of the cross section. Note that the values for the cross sections and their errors (especially the uncertainties in the systematics) are still preliminary and may change slightly in the final result.

13 Comparison with other measurements and theoretical calculations

Our measured cross section can be compared with the cross section evaluated by the UA1 Collaboration for the dimuon production through $p\bar{p}$ collisions at the centre of mass energy $\sqrt{s} = 630\ GeV$ [17]:

$$\sigma(p\bar{p} \rightarrow \mu^+\mu^- + X\ ;\ M_{\mu^+\mu^-} > 11\ GeV/c^2) = (240 \pm 40 \pm 50)\ pb.$$

A theoretical calculation of the Drell-Yan cross section was performed by Altarelli et al. [18]. This calculation yields for $\sqrt{s} = 540\ GeV$ and $M_{ee} > 12\ GeV$:

$$\sigma(p\bar{p} \rightarrow e^+e^- + X\ ; M_{ee} > 12.0\ GeV and \sqrt{s} = 540\ GeV) = (230 \pm 70)\ pb.$$

In order to compare our measurement with the theoretical calculation, we scale the value obtained by Altarelli et al. by the ratio of the calculated cross section for the production of W through $p\bar{p}$ collisions at $\sqrt{s} = 540\ GeV$ and $\sqrt{s} = 630\ GeV$ (≈ 1.28) [20]. Furthermore, we extrapolate the calculated Drell-Yan cross section to $M_{ee} > 10.0\ GeV$. The uncertainties of this method is $\approx$10 %. The dashed line on figure 26 represents this scaled value, whereas the full line corresponds to the Drell-Yan cross section calculated at $\sqrt{s} = 540\ GeV$. The two striped area correspond to the errors in the calculation of the Drell-Yan cross section. In addition, figure 26 shows the Drell-Yan cross sections measured by UA2 and UA1.

If we evaluate the Drell-Yan cross section in the invariant mass interval $26\ GeV/c^2 < M_{ee} < 70\ GeV/c^2$ for $E_t > 5.5\ GeV/c$, we obtain:

$$\sigma(p\bar{p} \rightarrow e^+e^- + X) = (51 \pm 12 \pm 8)\ pb.$$

This value can be compared with the theoretical calculation done by Bettems et al. [19] (institue of theoretical physics of the university of Bern):

$$\sigma(p\bar{p} \rightarrow e^+e^- + X) = (47 \pm 5)\ pb.$$

This value is obtained for the invariant mass interval $26\ GeV/c^2 < M_{ee} < 70\ GeV/c^2$ by interpolation, calculated up to $\mathcal{O}(\alpha_s)$ terms and including the Sudakov exponentiation.

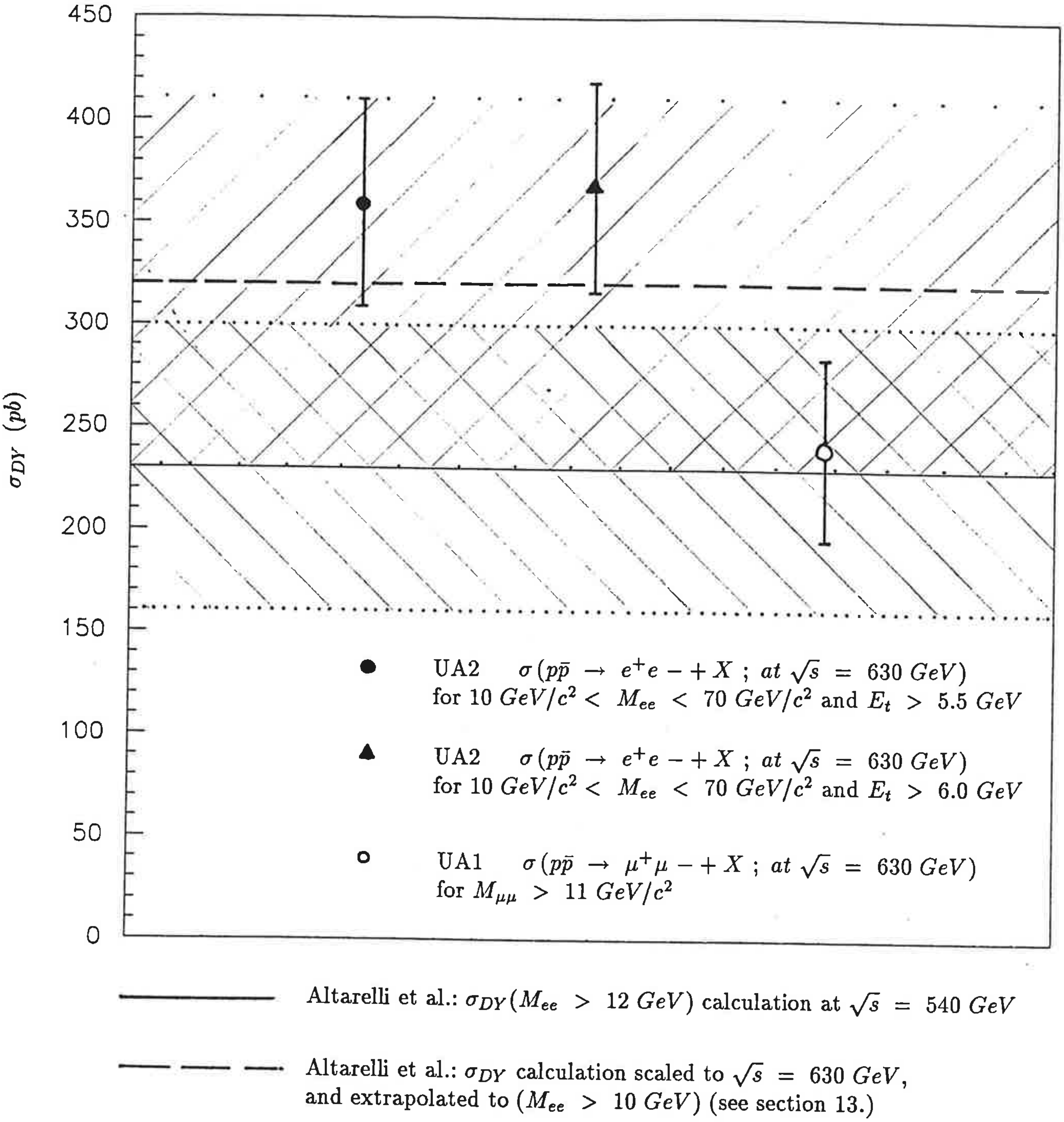

Figure 26: The measured cross sections for the production of Drell-Yan electron pairs is compared with the cross section obtained by the UA1 Collaboration and with that one, calculated by Altarelli et al. (full line) and scaled (dashed line, see description in section 13). The two striped area correspond to the errors in the Drell-Yan cross section calculation.

References

[1] A. Beer et al. Nucl.Inst.Meth 224 (1984) 360

[2] The UA2 experiment at ACOL, CERN-EP/87-78

[3] J.H. Christenson et al. Phys.Rev.Lett. 25: 1523(1970)

[4] R. Ansari et al. Nucl.Inst. Meth. A279 (1989) 388

[5] F. Bosi et al. CERN-EP/89-82

[6] K. Borer et al. Nucl.Inst. Meth. A253 (1987) 548

[7] K. Borer et al. Nucl.Inst. Meth. A286 (1990) 128

[8] Measurement of W and Z production cross section at the CERN $p\bar{p}$ collider; the UA2 Collaboration, CERN-EP/90-20

[9] J. Alitti et al. Nucl.Inst.Meth. A(1989) 364

[10] UA2 Collaboration, "Proposal to improve the Performance of the UA2 Detector CERN/SPSC 84-30 SPSC/P93 Add.2 15 May 1985

[11] I.R. Kenyon CERN-EP/82-81

[12] S.D Drell T. Yan Phys.Rev.Lett. 25, (1970) 1523

[13] R.K Ellis note from the CERN Scool of Physics 1989

[14] G. Altarelli CERN-TH/5290/89

[15] H.U. Bengtsson and T. Sjöstrand LU-TP 87-3 UCLA-87-001

[16] H.U. Bengtsson, Computer Physics Communications 31, (1984) 323

[17] notes from the 8th $p\bar{p}$ workshop 1989, Castiglione della Pescaia, Italy

[18] G.Altarelli et al. CERN-TH/4015

[19] J.M Bettems et al. inclusive lepton pair production through virtual W,Z and γ gauge Bosons in proton-antiproton collisions. BUTP-90/13,to be published.

[20] P. Minkowsky, talk given at the "Workshop on Physics in the 90's at the SPS Collider", Zinal (Switzerland) 1985, 181

[21] P. Nason et al. ETH-PT/89-2, Fermilab-PUB-89/91-T

[22] C. Albajar et al. Phys.lett B 213 (1988) 405

[23] T. Matsuura et al. Phys.lett B 211 (1988) 171

[24] R.K. Ellis 1th proc. of the Moriond workshop (1981) 231

[25] F. James M. Roos MINUIT function minimazation and error analysis CERN DD/D506

[26] E. Eichten et all., Rev.Mod.Phys. 56, (1984) 579

Acknowledgement

I would like to acknowledge Prof. Dr. K. Pretzl, who allowed me to complete my Ph.D. work in the UA2 Collaboration.

I thank Prof. Dr. E. Hugentobler for his spontaneous discussions during the last few years.

I thank my supervisor PD Dr. J. Schacher for the stimulating discussions we had and for the suggestions he gaved to me.

I would like to thank Dr. T. Pal for his admirable and patient efforts in teaching the art of analysis in this complex field. This work was substantially motivated by him. We spent a incredible amount of time together at CERN and we had a lot of fun in completing this work.

I thank Dr. P. Schwab for his help and support in all what concerned computing and Dr. L. Müller for his help in all subtle mathematical problems. Furthermore I thank them for the relaxed and spontaneous talks we often had.

I thank Prof. P. Minkowsky for the theoretical discussions and suggestions during this work. I also thank his students J.P. Bettems and Ch. Greub for the theoretical calculations.

I thank the whole UA2 collaboration for allowing me to participate in such a challanging experiment.

I thank the whole technical and mechanics stuff of the Bern high energy physics group for their contribution to the UA2 experiment.

Curriculum vitae

I was born on the 2th January 1956 in Merano (Italy) wher I lived till 1964.

I attended the basic scool in Ostermundigen (a suburb of Bern) till 1972.

During the period of 1972 to 1975 I succesfully passed the apprenticeship in the Union Bank of Switzerland at Bern.

Between 1975 and 1978 I attended the secondary scool.

1979 I enroled in the University of Berne where I started to study physics as a main subject with the subsidiaries mathematics and chemistry.

I started my work in the field of high energy particle physics in the year 1983, where I first joined the PSI group, who at that time was involved in an experiment for the precision measurement of the branching ration $(\pi \rightarrow e\nu)/(\pi \rightarrow \mu\nu)$ with an accuracy of a few 0.1 %.

I finished the diploma work in the year 1987 and started immediatly with my Ph.D. thesis as a member of the UA2 collaboration under the Bern group.

Addendum

The determination of the CALELE efficiency has been completed [1], and the values we use for the calculation of the cross section corresponds to the equivalent of superimposing 1.7 minimum bias events. This is summarized in the following table:

Table 25: Results of the CALELE efficiency for 10 *GeV* electrons with 1.7 minimum bias events superimposed.

cell type	*efficiency* (in %)
central cells	85.6 ± 0.9
edge cells	70.5 ± 6.2

Furthermore, the efficiency of the TOF counters, $\varepsilon_{TOF} = 98.4 \pm 0.4$ % is included in the calculation of the cross section.

The value of the cross section for electron pairs, produced through $p\bar{p}$ collisions at the centre of mass energy $\sqrt{s} = 630\ GeV$, in the mass interval $10\ GeV/c^2 < M_{ee} < 70\ GeV/c^2$ is:

$$\sigma\,(p\bar{p} \rightarrow e^+e^- + X\,) = [389 \pm 56\ (stat.) \pm 60\ (syst.)\,]\,pb$$

The calculation of the differential cross section for $p\bar{p} \longrightarrow \gamma^\star/Z^0 \longrightarrow l^+l^-$ with the $\gamma^\star/Z^0$ interference has been provided by T. Matsuura [2]. The computation of the cross section takes into account the dominant second order correction terms to the lepton pair production. The data sample, divided in four mass intervals, is compared to the predicted differential cross section $(d\sigma/dM)$ for the same mass intervals. The results are shown in figure 27 where only the statistical errors have been indicated for the data.

We plot $m^3\ d^2\sigma/dm\ dy$ at $y = 0$ versus the scaling variable $\sqrt{\tau} = m/\sqrt{s}$, and compare to previous measurements [3][4][5][6][7]. This comparison is shown in figure 28 where an approximate scaling is observed.

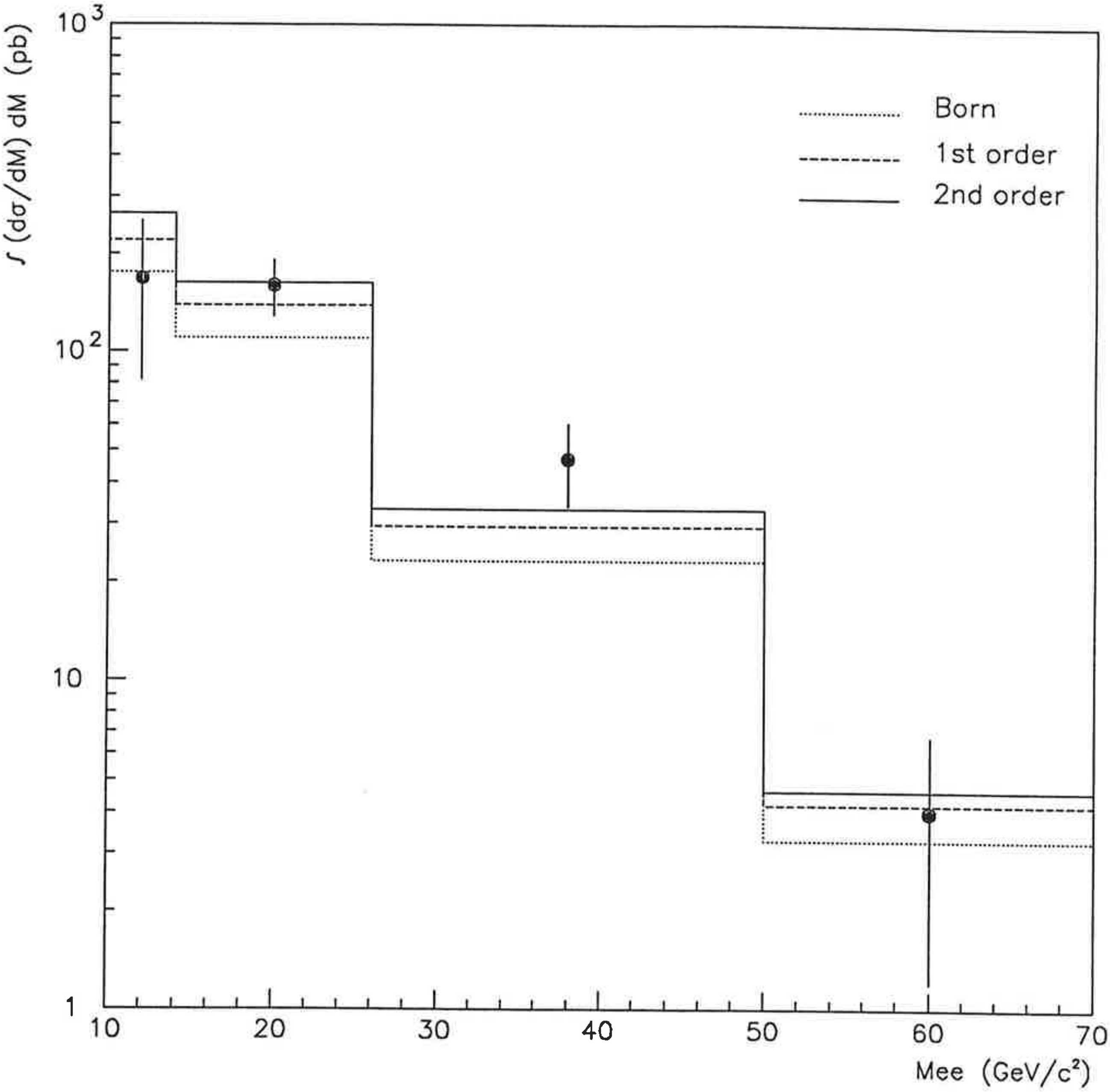

Figure 27: The values of the cross section in four mass intervals, compared to the theoretical predictions of ref. 1 (see text).

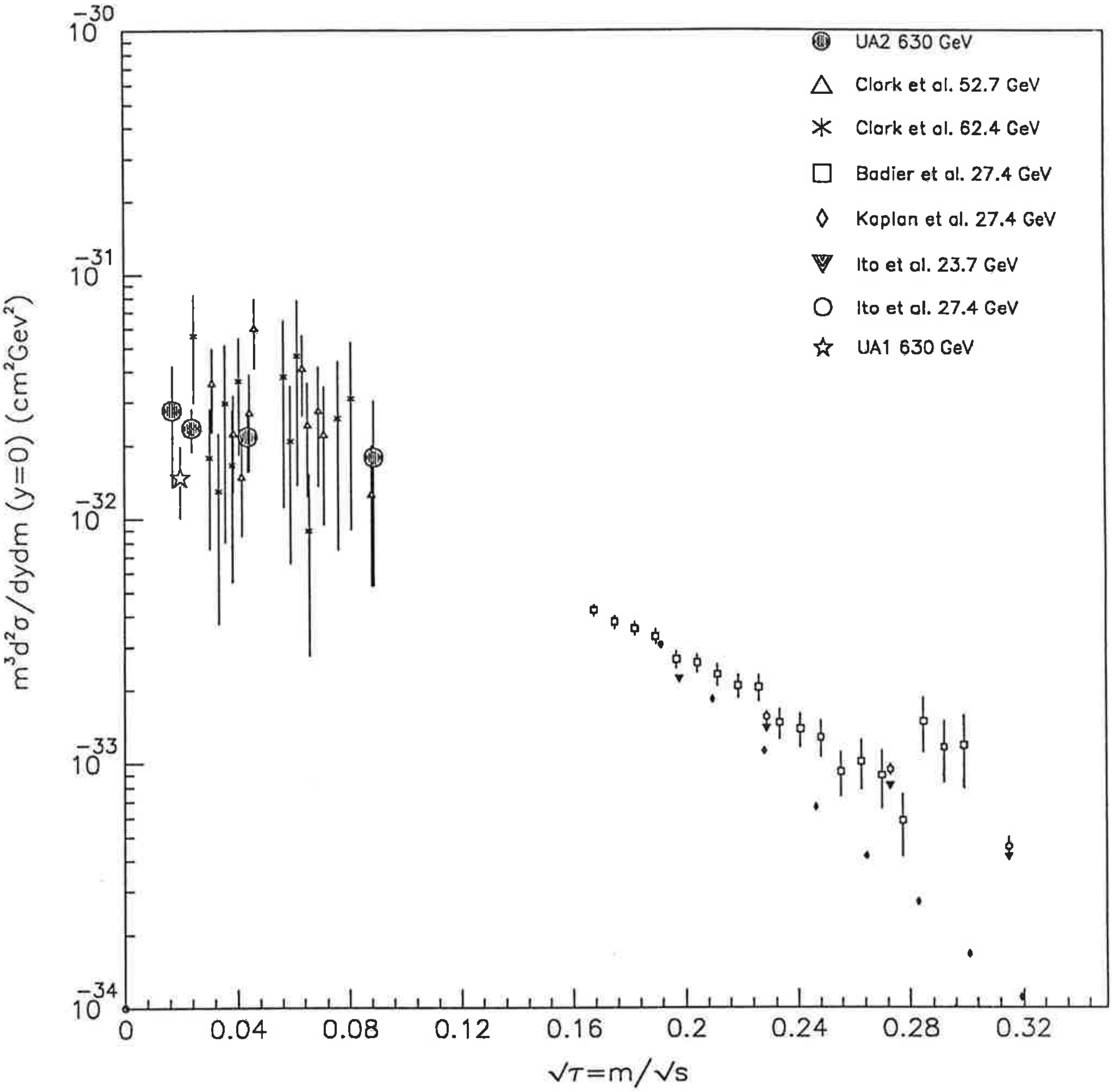

Figure 28: The Drell-Yan cross section as a function of the scaling variable $\sqrt{\tau} = m/\sqrt{s}$, compared to previous measurements.

References

[1] A. Federspiel, J. M. Gaillard and T. Pal, UA2 internal note ($p\bar{p}$ note #607, 11. August 1990)

[2] T. Matsuura et al. Phys.lett B 211 (1988) 171

[3] A.G. Clark et al. Nuc.Phys. B 142 (1978) 29

[4] J. Badier et al. Z.Phys C 26 (1985) 489

[5] D.M. Kaplan et al. Phys.rev.lett 40 (1978) 435

[6] A.S. Ito et al. Phys.rev D 23 (1981) 604

[7] C. Albajar et al. Phys.lett B 186 (1987) 237